JOURNAL OF PETROLOGY

Journal of Petrology, 2017, Vol. 58, No. 3, 443–472
doi: 10.1093/petrology/egx022
Advance Access Publication Date: 29 May 2017
Original Article

OXFORD

A Branched Magma Feeder System during the 1669 Eruption of Mt Etna: Evidence from a Time-integrated Study of Zoned Olivine Phenocryst Populations

Maren Kahl[1,2,3]*, Marco Viccaro[4,5], Teresa Ubide[6,7], Daniel J. Morgan[3] and Donald B. Dingwell[2]

[1]Institute of Earth Sciences, University of Iceland, Sturlugata 7, IS-101 Reykjavík, Iceland; [2]Department of Earth & Environmental Sciences, LMU Munich, Theresienstrasse 41, 80333 München, Germany; [3]School of Earth & Environment, University of Leeds, Leeds LS2 9JT, UK; [4]Università di Catania, Dipartimento di Scienze Biologiche Geologiche e Ambientali – Sezione di Scienze della Terra, Corso Italia 57, I-95129 Catania, Italy; [5]Istituto Nazionale di Geofisica e Vulcanologia, Osservatorio Etneo, Piazza Roma 2, I-95125 Catania, Italy; [6]Department of Geology, Trinity College Dublin, Dublin 2, Ireland; [7]School of Earth and Environmental Sciences, The University of Queensland, Brisbane, QLD 4072, Australia

*Corresponding author. Present address: Institute of Earth Sciences, University of Iceland, Sturlugata 7, IS-101 Reykjavík, Iceland. Telephone: +354 525 4481. E-mail: marenk@hi.is

Received July 5, 2016; Accepted April 12, 2017

ABSTRACT

The 1669 eruption of Mt Etna was one of the most voluminous and devastating of its flank eruptions in historical times. Despite a large body of relevant research, knowledge of the timing and duration of magma transfer and magma recharge through the internal plumbing system preceding and during the eruption is still limited. To address that lack of knowledge, we apply a three-way integrated method, linking systems analysis of crystals, a time-integrated study of zoned olivine populations, and a forward-modelling approach using thermodynamic calculations. Analysis of 202 olivine crystals erupted during the initial (pre-March 20, i.e. SET1) and the final (post-March 20; i.e. SET2 and MtRs) stages of the eruption reveals the existence of three magmatic environments (MEs) in which the majority of the olivine cores [M_1 (= $Fo_{75–78}$)] and rims [i.e. M_5 (= $Fo_{51–59}$) and M_3 (= $Fo_{65–69}$)] formed. Application of the rhyolite-MELTS software allowed us to constrain the key intensive variables associated with these MEs. We find that temperature, water content and oxidation state vary between these MEs. Application of diffusion modelling to the zoned olivine crystals allowed us to reconstruct the timing and chronology of melt and crystal transfer prior to and during the 1669 flank eruption. We find that, following the formation of the olivine cores [M_1 (= $Fo_{75–78}$)], the reservoir M_1 was intruded by batches of more evolved, degassed and possibly aphyric M_5-type magma, commencing 1·5 years prior to eruptive activity. This is the origin of the SET1 olivine rims (i.e. $Fo_{51–59}$). In the months prior to eruption, timescale data show that recharge activity along the newly established pathway M_1–M_5 increased notably. Starting in November 1668, only a few weeks after the first intrusive episode into the M_1 reservoir, a second pulse of magma injections (M_3-type magma) occurred and a new pathway M_1–M_3 opened; this is how the SET2 olivine rims (i.e. $Fo_{65–69}$) formed. For several weeks a bifurcated transport system with two dominant magma pathways developed along M_1–M_5 and M_1–M_3 dyke injections. Accompanied by vigorous seismicity, in the days immediately before eruption the local magma transfer dynamics changed and the M_1–M_5 recharge activity slowed down, as shown by a relative lack of crystals recording shorter timescales. M_1–M_3 recharge, however, remained high and persisted following the eruption onset on March 11, during which the SET1 lavas were drained. We propose that the change of the local

© The Author 2017. Published by Oxford University Press. All rights reserved. For Permissions, please e-mail: journals.permissions@oup.com

magma transfer dynamics might be linked to changes in the local stress field brought on during eruption. This may potentially have been due to repeated dyke injections into Etna's shallow plumbing system disrupting the early M_1–M_5 pathway and at the same time stabilizing the M_1–M_3 route as a dominant feeder. This transfer of system feeding would reproduce the observed syn-eruptive recharge and mixing in the weeks following eruption onset, culminating in the eruption of the later SET2 lavas.

Key words: olivine zoning; plumbing system; Mt Etna; timescales; magma mixing

INTRODUCTION

Geological setting

Mount Etna is a 3340 m high (above sea level; a.s.l.), composite stratovolcano located on the eastern coast of Sicily (Fig. 1) and covering a basal area of ~1250 km^2. It is located at the intersection of three tectonic domains, bounded by the transform Malta escarpment to the east, the Hyblean Plateau to the south and the subduction-related Aeolian arc to the north. To the west, subduction is blocked by compressive continental collision between the European and the African plate. Numerous models, including the southward migration of the Ionian slab (e.g. Schiano *et al.*, 2001) and the opening of a slab window (Gvirtzman & Nur, 1999; Doglioni *et al.*, 2001) have been proposed to explain the anomalous location of the volcano close to the suture zone of the African and European plates and its high magmatic flux. Geologically, the volcano rests on the southern edge of the overthrust units of the Apennine–Maghrebian chain to the south (Fig. 1), and the undeformed remnants of the African margin to the SE (e.g. Branca *et al.*, 2011). Volcanism is constrained to have started in the Etna region about ~500 kyr ago (Gillot *et al.*, 1994; Branca *et al.*, 2011).

Types of eruptions at Mt Etna: summit vs flank activity

Like other basaltic stratovolcanoes, Etna is characterized by summit and flank eruptions. Summit eruptions are usually constrained to one of six central craters (Voragine, Bocca Nuova 1, Bocca Nuova 2, Northeast Crater, Southeast Crater and New Southeast Crater) and the sub-terminal area (e.g. Branca & Del Carlo, 2004; Allard *et al.*, 2006; Corsaro *et al.*, 2009). Flank eruptions usually affect the intermediate and lower flanks of the volcano and can produce lava flow fields of considerable extent (e.g. the 1991–1993 flank eruption produced a compound lava flow field of $(240 \pm 29) \times 10^6$ m^3; Calvari *et al.*, 1994; Stevens *et al.*, 1997). Two types of flank eruptions have been defined: (1) central–lateral (Rittmann, 1965) or Central Conduit-Fed (CCF; Corsaro *et al.*, 2009); (2) eccentric (Rittmann, 1965), peripheral (Acocella & Neri, 2003) or Deep Dyke-Fed (DDF; Corsaro *et al.*, 2009) eruptions. Central–lateral flank eruptions originate by fracturing and lateral draining of the central conduits with the formation of eruptive vents at high altitudes. The eruption products resemble closely those erupted from the summit craters in being highly porphyritic (~30–40% crystals) and plagioclase-rich owing to significant water degassing in the central conduit system (e.g. Métrich *et al.*, 2004). Eccentric or DDF flank eruptions occur rarely [1763 (Corsaro *et al.*, 2009); 1974 (Corsaro *et al.*, 2009), 2001 (Behncke & Neri, 2003; Lanzafame *et al.*, 2003; Métrich *et al.*, 2004; Corsaro *et al.*, 2007; Ferlito *et al.*, 2012) and 2002–2003 (Andronico *et al.*, 2005; Spilliaert *et al.*, 2006)]. Eccentric eruptions are highly explosive with high tephra/lava ratios (e.g. Andronico *et al.*, 2005), and have low to medium phenocryst contents (<20%; Andronico *et al.*, 2005), with dominantly mafic mineral phases (Armienti *et al.*, 1988; Corsaro *et al.*, 2009; Ferlito *et al.*, 2012). As these eruption products differ from those of summit and CCF flank eruptions, previous studies concluded that eccentric eruptions must have been driven by rapid ascent of deeply rooted intrusions—below the volcanic pile—that bypassed the shallow, central conduit system and therefore are undegassed (e.g. Corsaro *et al.*, 2009; Ferlito *et al.*, 2012). Hence, this type of flank eruption is also referred to as Deep Dyke-Fed (DDF; Corsaro *et al.*, 2009), as opposed to the more common central–lateral or Central Conduit-Fed (CCF; Corsaro *et al.*, 2009) flank eruptions.

The 1669 eruption: characteristics and historical context

Here, we focus on the 1669 eruption, which is a central–lateral or Central Conduit-Fed flank eruption. The 1669 eruption was ranked as one of the most destructive and voluminous [$(607 \pm 105) \times 10^6$ m^3; Branca *et al.*, 2013] flank eruptions of Mt Etna in historical times (e.g. Corsaro *et al.*, 1996; Branca *et al.*, 2013). Between 1607 and 1669, eight flank eruptions occurred on different sectors of the volcano; a brief summary of the duration, location of eruption vents and erupted volume is provided in Table 1. Preceded by a period of summit eruptions between 1654 and 1656 (http://www.ct.ingv.it/en/11-notizie/news/561-etna-eruptions-pre1900.html) and more than 2 weeks of increasing seismic activity (e.g. Corsaro *et al.*, 1996, and references therein), the 1669 eruption commenced in the early morning of March 11 through a system of NNW–SSE-trending eruptive fissures that opened between 950 and 700 m a.s.l. (indicated as 1 in Fig. 1; Branca *et al.*, 2013). This first segment of the eruptive fracture system was characterized by weak and short-lived explosive activity.

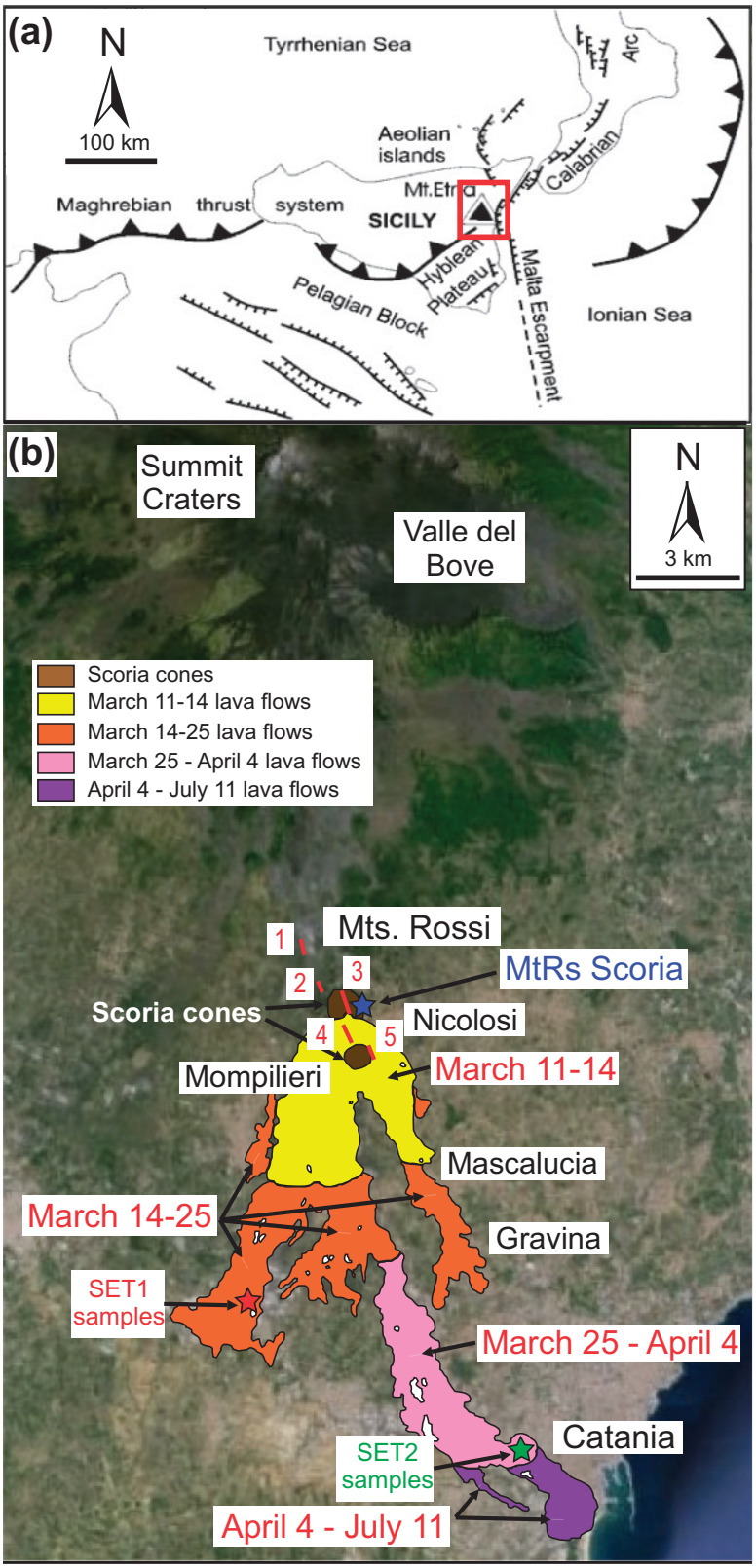

Fig. 1. (a) Location and geodynamic setting of Mt Etna with respect to the Apennine subduction front, the Malta escarpment (dashed line) and the subduction-related Aeolian island arc to the north. (b) Digital map of the south flank of Mt Etna illustrating the spatial distribution of the 1669 lava flow front and the progressive opening of the eruptive fissures (1–5). The different lava flow units are illustrated in distinct colours to highlight the temporal evolution of the flow field. Sample localities of the SET1 (1-6/10) and SET2 (2-1/5) lava flows and the MtRs bomb are marked with stars.

Table 1: Summary of 17th century flank activity

Flank eruption	Location and notes	Volume and length	References
1607 (June 28–?)	NW flank (2500–1500 m?); fissure above Monte Spagnolo cinder cone	Volume n.d.; lava flow of ~5 km	1–3
1610 (1st phase February 6–May 3; 2nd phase May 3–August 15)	1st phase: SSW flank (2800–2200 m); Grotta degli Archi craters; 2nd phase: SW flank (2300–1700 m); large lava flows near Adrano	Total volume of lava flows: 120×10^6 m^3 (1st phase 30×10^6 m^3; 2nd phase 90×10^6 m^3); total volume of pyroclastic material: $<4 \times 10^6$ m^3 (1st phase 3×10^6 m^3; 2nd phase $<1 \times 10^6$ m^3); total length of lava flow field: 11 km	1–4
1614 (July 1)–1624 (?)	N flank (~2500 m); most of the eruptive fissure is buried under younger lavas, but two larger cones (Due Pizzi) remain visible	Total volume of lava flows: ~1 km^3; total volume of pyroclastic material: 2×10^6 m^3; complex lava flow field up to ~9 km in length	1–3
~1630	NW flank from a fissure at 2250 m elevation, emitting 'Val di Cannizzola' lava flow; another small lava flow located higher upslope was erupted from a fissure just below Punta Lucia	n.d.	
1634 (December 18)–1636 (June)	SE flank (2090–1975 m); short fissure formed a row of hornitos and lava flows, causing damage in the area above Zafferana and threatening the village of Fleri	Total volume of lava flows: 180×10^6 m^3; total volume of pyroclastic material: 1×10^6 m^3; length of lava flow field: ~9 km, divided into two branches	1–4
1643 (February)	NE flank (2000–1700–1380–1350–1250 m); this is probably one of the smallest flank eruptions of Etna, characterized by a NE–SW and NNE–SSW fracture system that produced small lava flows	Total volume of lava flows: ~1×10^6 m^3 ?; length of lava flows: up to ~5 km	1, 2
1646 (November 20)–1647 (January 17)	NNE flank (1950 m); intense Strombolian activity formed the Mt Nero scoria cone, and lava flows causing damage to cultivated areas	Total volume of lava flows: 160×10^6 m^3; total volume of pyroclastic material: 7×10^6 m^3; lava flow up to ~7 km long	1–3, 5
1651 (January 17)–1653 (?)	W flank (2500–2120 m); lava flows partially destroyed Bronte and caused damage. The lava flow-field has many areas of ropy pahoehoe, a rather rare lava type on 1651 on the eastern flank (Macchia di Giarre) and was covered by the 1689 lava	Total volume of lava flows (only western flank): 500×10^6 m^3; lava flow field up to ~14 km long	2, 3, 6
1669 (March 11–July 11)	S flank (850–700 m); development of a NNW–SSE-oriented fracture system 14 km long (from Mt Frumento Supino, 2800 m to Mompilieri, 600 m). Vigorous Strombolian activity formed the Mts Rossi scoria cones. Lava effusions divided into three main branches that destroyed La Guardia, Belpasso, Mompilieri, Camporotondo, S. Pietro Clarenza, Massa Annunziata, S. Giovanni Galermo, Misterbianco and western part of Catania	Total volume of lava flows: $>600 \times 10^6$ m^3; total volume of pyroclastic material: from 80×10^6 to 250×10^6 m^3; lava flow field up to ~17 km long covering an area of 40 km^2	1–3, 6–9

n.d., not determined. References: 1, Recupero (1815); 2, Branca & Del Carlo (2004); 3, Tanguy *et al.* (2007); 4, Carrera (1636); 5, Ferrara (1818); 6, Mancino (1669); 7, Borelli (1670); 8, Branca *et al.* (2015); 9, Mulas *et al.* (2016).

A second segment (2) opened shortly afterwards between 850 and 825 m a.s.l. and built a spatter rampart (Fig. 1). That same day (March 11) a third segment (3) opened between 850 and 775 m a.s.l. This became the main vent—Mt Rossi—of the eruption (Fig. 1) and initially produced extended, explosive activity with ash fall followed by lava emission. The fourth segment (4) formed between 750 and 700 m a.s.l. close to the cone of Mt Mompilieri (Fig. 1; Branca *et al.*, 2013); it was characterized by mild explosive activity and a minor lava flow. On March 12 a fifth segment (5) formed at the eastern base of Mt Mompilieri between 700 and 640 m a.s.l. (Branca *et al.*, 2013). The eruptive activity continued for 122 days and destroyed several towns and settlements along the south flank of Etna volcano until it ceased on July 11, 1669. Activity at the summit craters remained quiet during the flank eruption until March 25, when a violent explosive event occurred followed by the partial collapse of the summit cone (Corsaro *et al.*, 1996; Nicotra & Viccaro, 2012). A detailed report of the sequence of events and the evolution of the lava flow field during the 4 months of eruptive activity has been given by Branca *et al.* (2013).

In comparison with some of the historical and recent flank eruptions (e.g. 1991–1993), the 1669 eruption was relatively short-lived, with only 4 months of eruptive activity. During this brief interval of persistent eruptive activity, a compound lava flow field covered a total area of ~40×10^6 m^2, with a total length of 17 km (Branca *et al.*, 2013). The relatively low altitude (800–850 m a.s.l.) of

the erupting vents and high effusion rates (58 ± 10 m^3 s^{-1}; Branca *et al.*, 2013) allowed the lava flows to run over long distances. As a result, settlements located on the lower southern flank of the volcano, including the western districts of Catania, were destroyed (e.g. Branca *et al.*, 2013). The 1669 flank eruption marks a major transition in terms of eruption intensity and petrography amongst the historical lavas (Tanguy, 1980; Guest & Duncan, 1981; Clocchiatti *et al.*, 1988; Hughes *et al.*, 1990; Condomines *et al.*, 1995; Corsaro *et al.*, 1996). Pre-1669 eruptions (1600–1669) were long-lasting, porphyritic and plagioclase-rich with high mean effusion rates (1·19 m^3 s^{-1}; e.g. Hughes *et al.*, 1990; Nicotra & Viccaro, 2012; Branca *et al.*, 2013). In contrast, the post-1669 eruptions (1670–1755) were more sporadic and short-lived and had low output rates (0·02 m^3 s^{-1}; Branca *et al.*, 2013). Post-1669 eruption products also contain predominantly mafic phase assemblages (Corsaro *et al.*, 1996).

It is possible that the steady increase in effusion rates during the first half of the 17th century culminated in the devastating March–July 1669 flank eruption. It has been argued that lateral draining of the central conduit system during the eruption caused not only the partial collapse of the summit cone (e.g. Corsaro *et al.*, 1996), but also had long-lasting consequences for the evolution of Etna's shallow plumbing system (e.g. Condomines *et al.*, 1995). The impact of Etna's modified shallow plumbing configuration could be observed in the century following the 1669 eruption, with the 1670–1755 period displaying significantly lowered output rates (0·02 m^3 s^{-1}; Branca *et al.*, 2013) and sparse flank activity (only three flank eruptions). It was only afterwards, in the period 1755–1970, that the mean effusion rate increased steadily to 0·51 m^3 s^{-1} (e.g. Branca *et al.*, 2013, and references therein).

Detailed geochemical and petrological studies of the products of the 1669 eruption (Corsaro *et al.*, 1996) revealed that the erupted lavas are porphyritic hawaiites containing variable amounts of phenocrysts [porphyritic index (PI) = 37–52 vol. % phenocrysts] and mafic mineral phases [mafic mineral phenocrysts/total phenocrysts; phenocryst colour index (CI_{Phx}) = 10–53 vol. %]. Corsaro *et al.* (1996) found that the lavas erupted during the initial stages of the 1669 eruption (i.e. between March 11 and 20) differ considerably in their petrography (i.e. average PI = 33 and CI_{Phx} = 36 vol. %) from lavas erupted after March 20 (average PI = 44 and CI_{Phx} = 18 vol. %). Petrographic differences are also reflected in the major and trace element bulk geochemistry (Barbieri *et al.*, 1993; Corsaro *et al.*, 1996). Consequently, Corsaro *et al.* (1996) classified the 1669 lavas into two groups: SET1 and SET2.

SET1 products were emplaced during the initial phase of the eruption, from March 11 to March 20, 1669. These samples have been described as being more 'basic' and 'magnesian', with similarities to later 18th and 20th century eruption products. SET1 bulk-rock compositions from Corsaro *et al.* (1996) are characterized by higher MgO (mean 6·65 ± 0·38 wt %) contents and higher compatible (i.e. Cr, Ni, Co, Sc) and incompatible (e.g. Th, La) trace element concentrations than the later erupted SET2 lavas (Corsaro *et al.*, 1996). The SET2 samples were emplaced after March 20, 1669 and were described by Corsaro *et al.* (1996) as plagioclase-phyric and more evolved in composition (e.g. mean MgO 5·07 ± 0·19 wt %) than the SET1 eruption products. SET2 lavas strongly resemble the plagioclase-phyric rocks of the early 17th century (Corsaro *et al.*, 1996).

Both sets of eruption products (SET1 and SET2) were interpreted by Corsaro *et al.* (1996) as the result of fractional crystallization of two compositionally distinct primary magmas under distinct storage conditions, which fractionated different volumetric proportions of phenocrysts. Corsaro *et al.* explained segregation by utilizing a 'laminar plume model', in which mafic, gas-rich and therefore buoyant SET1 magma rises through a pre-existing reservoir filled with SET2 melt, without significantly (physically or chemically) interacting with it; this allows uprising SET1 magma to retain its chemical and petrological signature, as mixing with SET2 melt is inhibited.

The possibility of fresh magma inputs being able to bypass resident, more viscous magma is not new; such a model was invoked by Landi *et al.* (2006) to explain the segregation of volatile-poor degassed magmas and volatile-rich 'golden pumices' during the April 5, 2003 paroxysm of Stromboli volcano. In this case, bubble-driven ascent of deep volatile-rich magma through shallower resident magma allowed rapid ascent to the vent, with subsequent mixing only after the paroxysm. Despite a possibly shared characteristic of magma injections not mixing in the first instance, the Stromboli and Etna systems are very different. A worrying implication of bypass behaviour is that intrusion and eruption can occur nearly simultaneously, and do not require a significant residence time of mafic magma in an evolved reservoir. This has considerable implications for the assessment of hazards posed by future 1669-type events, as it implies that similar, voluminous, low-elevation eruptions could commence with little warning. In fact, contemporary records indicate that signals of volcanic unrest in the form of vigorous seismic events, with epicenters located close to the town of Nicolosi on the southern flank of the volcano, preceded the 1669 eruption by ~2 weeks (e.g. Mulas *et al.*, 2016, and references therein); seismic activity increased on March 8, 1669, culminating in the eruption onset on March 11, 1669 (Tanguy & Patanè, 1996; Mulas *et al.*, 2016, and references therein). The purpose of this study is to obtain new insights into the plumbing system feeding the 1669 flank eruption and test viability (and hence hazard implications) of quick melt bypass.

Etna's modern (1991–2008) plumbing system: insights from a crystal chemistry perspective

In previous studies, Kahl *et al.* (2011, 2013, 2015) developed a novel petrological method linking a systems analysis approach to compositionally zoned olivine

populations with a time-integrated study (i.e. diffusion modelling in olivine). This approach was successfully applied to samples from recent summit and flank (i.e. 1991–2008) eruptions at Etna to reconstruct the residence and migration history of magma through its modern plumbing system (Kahl *et al.*, 2015). The present study uses and builds upon existing techniques and results developed by Kahl *et al.* (2011, 2013, 2015). Therefore, in this section, we review some of the main methods and concepts and briefly summarize what we know so far about Etna's modern plumbing system from a combined crystal chemistry and kinetic modelling approach.

Studying the compositional and zoning record of 180 olivine crystals that were erupted between 1991 and 2008 at Mt Etna, Kahl *et al.* (2011, 2013, 2015) recognized that zoning profiles of Fe–Mg and selected trace elements (e.g. Ni, Mn, Ca) in olivine contain core and/or rim compositional plateaux with diffuse boundaries separating them. The occurrence of such compositional plateaux was interpreted as sequential growth of olivine under a constant set of intensive thermodynamic variables (pressure, temperature, composition, fugacities of volatile species) defining a certain Magmatic Environment (ME). This is opposed to progressive changes, such as cooling or differentiation, that would result in continuous variations of composition rather than plateaux separated by sudden jumps or diffuse boundaries (Kahl *et al.*, 2015). An ME may represent a physically distinct entity (e.g. a sill, dyke), or a virtual entity (e.g. a set of P, T, X, fO_2, fH_2O conditions within a zoned larger magma reservoir). Kahl *et al.* (2011, 2013, 2015) used the terms 'magmatic reservoir' and 'magmatic environment' to distinguish the physical entity from the virtual entity defined by a set of intensive variables; the two may be the same (e.g. in an unzoned magma reservoir of small enough size) but do not have to be. Kahl *et al.* (2011) assumed that the compositional variation from core to rim in a crystal represents a chemical stratigraphy and that the compositional record can be used to identify and effectively track the different MEs crystals pass through on the way to eruption. Consequently, the change in zoning pattern from one plateau to another is equivalent to the transfer of the crystal from one ME to another. This can be accomplished either by the crystal physically moving (with some melt) from one environment to another, or by the environment itself changing around the crystal (e.g. by cooling or degassing). To be able to track effectively the sequence of magmatic events preserved in the chemical stratigraphy of populations of zoned olivine crystals, Kahl *et al.* (2011) developed the tool of systems analysis. This allows us to decipher the record of different pathways (sequences of changes in MEs) stored in the crystal cargo of a given rock by using connectivity diagrams to organize the compositional information. The frequency of connections found in the connectivity diagrams (diagrams where successive compositional plateaux are connected by directed line segments; the direction pointing from core toward rim) is taken to provide a measure of the relative frequency with which pathways between different environments were used. For example, Kahl *et al.* (2011) discovered that a single thin section of a lava flow from the 1991–1993 SE flank eruption of Etna contained olivine phenocrysts with three types of zoning patterns (normal, reverse and complex) and compositions ranging from Fo_{83} to Fo_{70}. Compositional plateaux in the olivine crystals were consistent with four MEs that, when considered with the relevant diffusive modifications, could be used to describe the total diversity of compositional variation in the olivine phenocrysts that were erupted between December 1991 and March 1992 (Kahl *et al.*, 2011). The width of the diffusion zone between two compositional plateaux and the shape of the concentration profiles record the duration and residence time a crystal spent within a given ME. Hence, Kahl *et al.* (2011) developed the tool of sequential kinetic modelling that allows the determination, working backward from the rim to the core, of the durations a crystal spent in different MEs prior to eruption. Finally, Kahl *et al.* (2015) developed a forward modelling approach using thermodynamic calculations with the MELTS software (Ghiorso & Sack, 1995; Asimow & Ghiorso, 1998) to identify the key intensive variables associated with the different MEs identified. In this approach the observed populations of mineral compositions (e.g. $Fo_{79–83}$) defining a certain ME (e.g. M_0), rather than single compositions, are associated with thermodynamic parameters (P, T, water content, oxygen fugacity and bulk composition of melt) to identify the most plausible set corresponding to each ME.

Application of this combined and novel method that links the crystal chemistry with a time-integrated study and forward thermodynamic modelling allowed Kahl *et al.* (2011, 2013, 2015) to investigate the temporal evolution of Etna's modern plumbing system across multiple eruptive episodes of different styles and at different locations. Considering the comprehensive compositional and zoning record preserved in 180 olivine crystals that erupted between 1991 and 2008, five MEs were identified: M_0 ($Fo_{79–83}$), M_1 ($Fo_{75–78}$), M_2 ($Fo_{70–72}$), M_3 ($Fo_{65–69}$) and mm_1 ($Fo_{73–75}$). Kahl *et al.* (2015) found that the same MEs as those deduced by Kahl *et al.* (2011, 2013) to describe the observed variability of olivine compositions erupted during the 1991–1993 flank and the 2006 summit eruptions could be used to describe the compositional variations recorded in all 1991–2008 olivine crystals. The combined systems analysis record of all eruption products revealed that although the MEs remained the same during the 17 years, the interconnectivity between them and hence the dominant magma pathways changed with time. The main changes were found either between large eruptions (1991–1993 and 2001) or between eruptive episodes.

For example, Kahl *et al.* (2013) studied the compositional and zoning record of olivines that were erupted

during two events (July 20 and October 28) of the 2006 summit eruptions at Mt Etna. They discovered that olivines of the July 20 and the October 28, 2006 eruptions were characterized not only by different zoning patterns, but also by different core and rim plateau compositions. The July 20 olivines were reversely zoned with low-forsterite core (= $Fo_{70–72}$) plateaux and higher forsterite rims (= $Fo_{73–75}$). Three months later, during the October 28 event, olivines showed dominantly normal zoning with high-forsterite core plateaux (= $Fo_{79–82}$) and decreasing forsterite contents at the rims (= $Fo_{70–72}$). Based on the different core and rim plateau compositions and the different zoning types (normal vs reverse) three MEs [M_0 (= $Fo_{79–82}$), M_2 (= $Fo_{70–72}$) and mm_1 (= $Fo_{73–75}$)] with diverging connectivity patterns were observed. Olivines erupted in July showed a dominant population of crystals connecting the environments M_2–mm_1, whereas olivines erupted in October tracked a different history connecting M_0–M_2. Kahl *et al.* (2013) argued that these different connectivity patterns revealed by the systems analysis of the 2006 olivine zoning and compositional record may be attributed to a small but significant change in the magma transport regime in the course of the 2006 eruption. They also concluded that such a change—which occurred within only months—may be explained best by a short-term change of the plumbing system sometime between July and October 2006. This agreed well with the observation that the July and October 2006 events occurred from different eruption centres.

By means of the systems analysis approach, Kahl *et al.* (2015) found that three dominant magma transfer routes connecting the environments M_0–M_1, M_2–mm_1 and M_1–M_2 have been active during the entire period (1991–2008). These MEs therefore represent robust and long-term features of Mt Etna's plumbing system that may have facilitated the transfer of magma to the surface for nearly two decades. In parallel, they also identified some sparsely frequented routes connected to more evolved MEs such as M_3 ($Fo_{65–69}$). Migration routes connected to this environment could be identified only in some eruption products and were therefore inferred to represent temporary pathways of magma transfer that were activated only occasionally or were traversed too quickly to be recorded in all olivine zoning profiles. The significance of such highly evolved but rarely tapped environments and their role in Etna's historical plumbing system will be evaluated further in this study. An important observation of Kahl *et al.* (2011, 2013, 2015) is the discovery of pre- and/or syn-eruptive pulses of mafic magma recharge into different MEs of the plumbing system, indicated by olivine populations with forsterite M_0 ($Fo_{79–82}$) core and/or rim compositions.

The application of sequential kinetic modelling revealed that the transfer of magma along the three most dominant routes in Etna's modern plumbing system M_0–M_1, M_2–mm_1 and M_1–M_2 occurred over heterogeneous timescales ranging from days to 2 years. Although some of the passageways have been sporadically active in the months and sometimes years before an eruption, the magma migration activity increased in the weeks and days prior to an eruptive event. For example, recharge of the environments M_1 and M_2 began years before an eruption, but became more frequent in the last few days prior to its onset (Kahl *et al.*, 2015). On the other hand, other environments such as mm_1 were found to represent transient features of Etna's modern plumbing system and formed within the last 40 days before eruptive activity commenced (Kahl *et al.*, 2015).

Kahl *et al.* (2015) concluded that temperature, water content and possibly oxidation state are the main distinguishing features of the different magmatic environments. They found that M_0 ($Fo_{79–83}$), the most primitive olivine population, may have grown with some clinopyroxene at high water contents (3·5–5·2 wt %) and fO_2 conditions buffered at quartz–fayalite–magnetite (QFM) or nickel–nickel oxide (NNO) at pressures ranging between 1·5 and 3·0 kbar (or even higher). Temperatures of >1110°C are required. The intermediate olivine population M_1 ($Fo_{75–78}$) could have formed over a broad spectrum of conditions, but all require lower water contents (0·1–1·4 wt %) at similar temperatures. The most evolved, Fe-rich olivines of M_2 and M_3 ($Fo_{70–72}$ and $Fo_{65–69}$) are the products of extremely dehydrated magmas (0·2–1·1 wt % H_2O for M_2; <0·5 wt % H_2O for M_3), and probably somewhat more reducing (QFM) conditions that were most probably obtained at even shallower depths and at somewhat lower temperatures (~1080°C).

The findings of multi-level magma transfer between different MEs within Etna's modern plumbing system derived by Kahl *et al.* (2011, 2013, 2015) agree with evidence from geophysical (e.g. Murru *et al.*, 1999; Aloisi *et al.*, 2002; Lundgren *et al.*, 2003; Patanè *et al.*, 2003, 2006, 2013; Bonaccorso *et al.*, 2011; Viccaro *et al.*, 2016*c*) and thermobarometric (e.g. Armienti *et al.*, 2013; Giacomoni *et al.*, 2014, 2016) studies. Thermobarometry calculations indicate that clinopyroxene starts crystallizing at depth >20 km (e.g. Armienti *et al.*, 2013; Giacomoni *et al.*, 2016) and continues to crystallize until eruption. The deep to intermediate crystallization range of clinopyroxene coincides with the detection of deep volcano-tectonic seismicity in the intermediate and lower crust (10–30 km; Patanè *et al.*, 2013) interpreted as periodic ascent of magma batches from the mantle (Patanè *et al.*, 2013). Plagioclase was found to start crystallizing at shallower depths in the upper crust (>12 km depth), with the majority nucleating around 5–6 km, and continues (like clinopyroxene) to crystallize until eruption (Viccaro *et al.*, 2010, 2016*a*; Giacomoni *et al.*, 2014, 2016). These crystallization levels coincide with the detection of low-velocity zones using seismic tomography (e.g. Murru *et al.*, 1999). The crystallization of both plagioclase and clinopyroxene seems to be continuous in a polybaric vertical feeding system, in which at least two magma crystallization levels have been identified (Armienti *et al.*, 2013; Giacomoni *et al.*, 2014, 2016).

This study

Here we apply the combined method developed by Kahl *et al.* (2011, 2013, 2015) to the 1669 eruption products, and investigate olivine zoning using novel imaging of crystallographic orientation and trace element distribution. Our aim is to (1) test the existence and duration of pre- and syn-eruptive mixing of SET1 and SET2 magmas, (2) obtain the residence times of SET1 and SET2 magmas within the plumbing system prior to eruption, and (3) reconstruct the pre- and syn-eruptive history of magmatic events leading to the 1669 flank eruption.

We first present a brief chronology of the eruption sequence, followed by descriptions of the relevant aspects of petrography and mineral chemistry, the types of zoning found in olivine and their major, minor and trace element compositional characteristics. We use these data to construct connectivity diagrams and carry out systems analysis, to determine the nature of magma transfer throughout the plumbing system. Then we undertake a forward-modelling approach of thermodynamic calculations using the rhyolite-MELTS software (Gualda *et al.*, 2012; Ghiorso & Gualda, 2015) to constrain the physical conditions of the identified MEs. Subsequently, we perform diffusion modelling to determine the timing and duration of magma mixing and magma migration between the MEs. Finally, we synthesize our findings and results to develop a conceptual model of the late-stage magmatic history before and during the 1669 eruption.

SAMPLES

A total of 10 lava samples and one bomb sample were studied, representing different episodes of the 1669 flank eruption. The locations of all samples studied are highlighted in Fig. 1 and the sampling locations and global positioning system (GPS) coordinates are listed in Table 2. We collected five lava samples from a flow unit that was emplaced on March 19, 1669. These samples were erupted before March 29 and therefore belong to the SET1 lavas as defined by Corsaro *et al.* (1996) (Fig. 1). Another five samples were collected from a lava flow that reached the outskirts of Catania (Fig. 1). This flow was emplaced after March 29 (possibly on April 4, 1669) and therefore falls into the SET2 lavas of Corsaro *et al.* (1996). The bomb sample was collected at the top of the Mt Rossi (MtRs) scoria cone (Fig. 1). An exact eruption date for this sample is not available, but given its location at the top of the cone that fed most of the eruption, we infer that it erupted towards the end of the volcanic activity and therefore also belongs to the SET2 category (erupted after March 20, 1669; Corsaro *et al.*, 1996).

ANALYTICAL METHODS

X-ray fluorescence (XRF)

Whole-rock compositions were determined by wavelength-dispersive X-ray fluorescence (WD-XRF) analysis (MagiX PRO XRF, Philips) at the Department for Earth & Environmental Sciences (DEES) at LMU. Major and minor elements were analyzed using glass beads prepared by fusion of 1 g sample and 9 g SPECTROMELT A12 (66% di-lithium tetraborate, 34% lithium metaborate) in a Panalytical Eagon 2 furnace fusion system at 1150°C. Analytical precision was checked against a basalt standard and reproducibility was found to be better than 0·15%.

Electron microprobe (EMP)

Olivine

Backscattered electron (BSE) images and detailed, quantitative concentration profiles (spacing ~4–5 μm) of major and minor elements (Si, Fe, Mg, Mn, Ca, Ni and Cr) along different directions in a total of 202 olivine crystals were obtained using a Cameca SX-100 electron microprobe (EMP) at the Ludwig-Maximilians Universität (LMU) Munich. Run conditions were 15 kV accelerating voltage, 20–30 nA beam current and a focused electron beam (1 μm) for the analysis of olivine. Peak and background counting times of 10 s were used for each element. Well-characterized synthetic oxides and minerals were used as analytical standards including (Si, Mg) olivine, (Ca) wollastonite, (Fe) almandine and andradite, (Mn) $MnTiO_3$, (Cr) Cr_2O_3 and (Ni) NiO.

Table 2: Sample locations

Sample	Latitude (°N)	Longitude (°E)	Location	Notes
SET1				
1–6	37·550439	14·986601	Piano Tavola	samples of lava emitted on March 19, 1669
1–7	37·550313	14·988188	Piano Tavola	samples of lava emitted on March 19, 1669
1–8	37·549912	14·988487	Piano Tavola	samples of lava emitted on March 19, 1669
1–9	37·549524	14·987525	Piano Tavola	samples of lava emitted on March 19, 1669
1–10	37·549245	14·986397	Piano Tavola	samples of lava emitted on March 19, 1669
SET2				
2–1	37·515367	15·041863	Catania San Nullo	samples of lava emitted after March 29 (possibly April 4) 1669
2–2	37·516550	15·041239	Catania San Nullo	samples of lava emitted after March 29 (possibly April 4) 1669
2–3	37·515609	15·043251	Catania San Nullo	samples of lava emitted after March 29 (possibly April 4) 1669
2–4	37·514929	15·043315	Catania San Nullo	samples of lava emitted after March 29 (possibly April 4) 1669
2–5	37·514670	15·042788	Catania San Nullo	samples of lava emitted after March 20 (possibly April 4) 1669
MtRs	37·61924	15·01103	Monte Rossi scoria cone	Monte Rossi scoria cone bomb, erupted after March 20 (possibly March 25) 1669

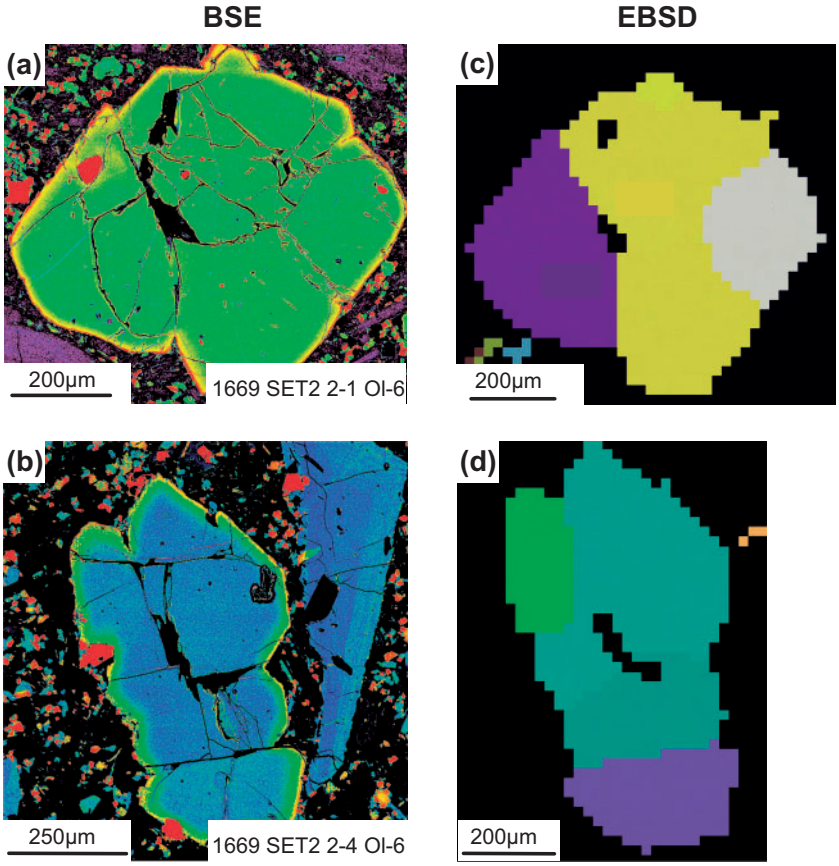

Fig. 2. Electron backscatter diffraction (EBSD) mapping of olivine. (a, b) False colour backscatter electron (BSE) images of olivine crystals that erupted during the second half (i.e. SET2) of the 1669 flank eruption. (c, d) Electron backscatter diffraction (EBSD) maps of the same crystals (i.e. 1669 SET2 2-1 Ol-6 and 2-4 Ol-6). Different colours in the corresponding EBSD maps refer to different orientations of the three measured Euler angles indicating different orientations of the crystallographic *a*-, *b*- and *c*-axes in the olivines. It should be noted that the application of EBSD mapping makes it possible to distinguish single crystals. Step sizes used for the EBSD orientation maps are 22·56 μm for 2-1 Ol-6 and 20·88 μm for 2-4 Ol-6.

Clinopyroxene

Major and minor element concentrations (Si, Fe, Mg, Mn, Ca, Ni, Na, Al, Ti, Cr and K) of 62 olivine–clinopyroxene pairs and single clinopyroxene crystals (spacing 3–6 μm) were obtained using a Cameca SX-100 EMP at LMU Munich. A total of 829 single spot analyses were made at 15 kV and 30 nA, using a focused beam (1 μm). The counting times at peak and background for each element were set to 10–20 s.

Fe–Ti oxides

Seventy-four single-point analyses across the contact zone between adjacent olivine and Ti-magnetite were made (Si, Fe, Mg, Mn, Ca, Ni, Na, Al, Ti, Cr and K) using a Cameca SX-100 EMP at LMU Munich. Run conditions were the same as for olivine.

Analytical quality was ensured by analysing reference materials as unknowns and by mineral stoichiometry calculations (Deer *et al.*, 2013).

Electron backscatter diffraction (EBSD)

Crystallographic orientations of olivine crystals were determined using electron backscatter diffraction (EBSD; Prior *et al.*, 1999; Costa & Chakraborty, 2004) on the FEI Quanta 650 FEGSEM at the University of Leeds Electron Microscopy and Spectroscopy Centre (LEMAS). Constraint of crystallographic directions in olivine with respect to the micro-analytical traverses is essential for accurate diffusion modelling, as the diffusivity of different elements (e.g. Fe–Mg or Ni) in olivine is strongly anisotropic, with diffusion along the *c*-axis being six times faster than that along the *a*- and *b*-axes (e.g. Clark & Long, 1971; Dohmen *et al.*, 2007).

To minimize uncertainty in the determination of the orientation data, orientation maps (Fig. 2c and d) consisting of hundreds of EBSD point determinations were conducted for each grain. Using the HKL CHANNEL5 EBSD post-processing software, orientation maps are generated over an entire crystal, extracting hundreds to thousands of single orientation measurements. This comprehensive approach is made possible by rapid acquisition and improves on earlier methods in which only a few points per olivine grain were measured. Because of the improved coverage and resolution, features such as internal lattice misorientations, sub-grain boundaries, twins and pseudo-symmetries can be easily identified. EBSD mapping of this type is novel and

has not been routinely used by the diffusion community so far. Details of the operating conditions are available as Supplementary Data Electronic Appendix 1 (Supplementary Data are available for downloading at http://www.petrology.oxford journals.org).

Laser ablation inductively coupled plasma mass spectrometry (LA-ICP-MS) mapping

The elemental distribution in seven olivine crystals was determined by laser ablation inductively coupled plasma mass spectrometry (LA-ICP-MS) mapping at the Geochemistry Laboratories of Trinity College, Dublin, according to the method developed by Ubide *et al.* (2015). The analyses were made on typical 30 μm thick polished sections of rocks from SET1, SET2 and the MtRs samples.

LA-ICP-MS mapping experiments were carried out using a Photon Machines G2 193 nm excimer Ar–F laser system with a Helex 2-volume ablation cell, coupled to a quadrupole Thermo iCapQc mass spectrometer. The carrier gas was a mixture of He and Ar (and minor N_2 introduced via an in-house developed variable volume smoothing device). The laser was operated with a fluence of 2·5 J cm^{-2}. The mapping area was built by overlapping ablation lines to form a rectangular grid. The laser spot size was determined by the size of olivine crystals and set at 10 μm. Ablation lines were built using a square laser mask, 15 μm s^{-1} scanning speed, 10 Hz repetition rate and 1 μm overlap between lines, following Ubide *et al.* (2015). A baseline measurement of 30–40 s was allowed between ablation lines. Given the typical bright colour of olivine grains in thin section, it was found that pre-ablation of the crystals using large, quick rasters (e.g. 85 μm circle laser beam, 160 μm s^{-1} scan speed, 20 Hz repetition rate, 1 μm overlap between lines) improved the ablation of olivine in the subsequent mapping experiment, producing sharper element maps. The analytes were ^{25}Mg, ^{27}Al, ^{29}Si, ^{31}P, ^{43}Ca, ^{45}Sc, ^{49}Ti, ^{51}V, ^{52}Cr, ^{55}Mn, ^{57}Fe and ^{60}Ni. Seven to 10 analytes were measured in each mapping experiment, with a total dwell cycle of 100–110 ms.

NIST612 glass reference material (Jochum *et al.*, 2011) was used at the beginning of each analytical session to tune the instrument. NIST610 glass reference material (Jochum *et al.*, 2011) was used as calibration standard for all mapping experiments. Data reduction and production of element distribution maps was undertaken with Iolite v2.5 free software (Paton *et al.*, 2011) using the 'Trace_Elements_Image' data reduction scheme (Ubide *et al.*, 2015). Following Chew *et al.* (2016), maps were initially built in 'Semi quantitative' mode and the scales were subsequently normalized to the Si content measured independently (38·5 wt % SiO_2 from olivine EMP data).

PETROLOGY

The 1669 eruption products are strongly porphyritic. The rocks contain the typical Etnean phenocryst assemblage of plagioclase (~12–15 vol. %), clinopyroxene (~8–11 vol. %), olivine (~3–5 vol. %), and accessory Fe–Ti oxides (~<3 vol. %) embedded in a fine-grained, hypo-crystalline groundmass. The groundmass consists of micro-laths of plagioclase, Fe–Ti oxides, clinopyroxene and variable amounts of interstitial glass. The abundances and relative proportions of phenocrysts (porphyritic index, PI) can vary significantly (PI ranging between 37 and 52%) between eruption products (see Corsaro *et al.*, 1996).

Plagioclase ($An_{56–85}$) forms mostly euhedral phenocrysts of variable size (0·2–4 mm). Plagioclase phenocrysts contain multiple sequences of oscillatory zoning as well as strong dissolution (sieve) textures (see also Corsaro *et al.*, 1996).

Clinopyroxene ($Wo_{46–48}$, $En_{36–41}$, $Fs_{13–16}$ and Mg# 73–93; see Supplementary Data Electronic Appendix 2) forms euhedral to subhedral phenocrysts with sizes ranging between 0·8 and 4·8 mm. Pronounced sector and oscillatory zoning and inclusions of Fe–Ti oxides are common; rare inclusions of plagioclase and olivine are also found.

Olivine ($Fo_{51–83}$; see Supplementary Data Electronic Appendix 3) is mostly subhedral or anhedral with slight dissolution features (e.g. rounded edges) and core–rim zonation. The size of olivine phenocrysts ranges between 0·2 and 1·5 mm.

Opaque Fe–Ti oxides ($Uvsp_{33–60}$, $Spn_{13–26}$, $Mt_{35–53}$; see Supplementary Data Electronic Appendix 4) form euhedral to anhedral phenocrysts or occur as inclusions in clinopyroxene and olivine crystals and in melt embayments.

Whole-rock compositions of SET1 and SET2 lava and the MtRs bomb sample (Table 3) are plotted in a total alkalis–silica diagram in Fig. 3a. For comparison, bulk-rock data fro SET1 and SET2 samples analysed by Corsaro *et al.* (1996) and Mulas *et al.* (2016) were added. The 1669 volcanic products are hawaiitic in composition. We observe that there is a compositional offset between our samples and some of the samples analysed by Corsaro *et al.* (1996). Mulas *et al.* (2016) have also reported a similar offset. Our SET1 and SET2 samples are relatively similar in composition to SET1 samples of Corsaro *et al.* (1996) and to the pyroclast samples studied by Mulas *et al.* (2016). In contrast, SET2 lavas of Corsaro *et al.* (1996) have higher SiO_2, Al_2O_3 and total alkalis (Fig. 3a–c) and lower TiO_2 and FeO contents (Fig. 3d and e). Our SET1 and SET2 samples have similar MgO contents (Fig. 3h–l) to the SET2 samples of Corsaro *et al.* (1996). According to the petrological descriptions of Corsaro *et al.* (1996), their SET2 samples contain abundant plagioclase phenocrysts and, as a result, have a generally lower phenocryst colour index (CI_{phx} = mafic mineral phenocrysts/total phenocrysts, vol. %; CI_{phx} = 18) than their SET1 samples (CI_{phx} = 36; see their fig. 2). Such plagioclase-rich rocks are common at Mt Etna and, when characterized by megacrystic plagioclase, are locally known as cicirara (see also Nicotra & Viccaro, 2012). Given that recent

Table 3: Bulk-rock compositions of SET1 and SET2 eruption products

	SET1				SET2				MtRs
	1–6	1–7	1–8	1–9	2–1	2–2	2–3	2–4	
wt %									
SiO_2	48·59	48·52	48·55	48·52	48·81	48·79	48·84	48·86	48·57
TiO_2	1·46	1·48	1·47	1·48	1·51	1·51	1·52	1·50	1·60
Al_2O_3	18·02	18·01	17·87	17·96	18·43	17·98	18·03	18·13	18·25
Fe_2O_3	10·09	10·06	10·07	10·04	10·17	10·27	10·37	10·28	10·72
FeO	9·08	9·05	9·06	9·03	9·15	9·24	9·33	9·25	9·65
CaO	10·47	10·47	10·54	10·58	10·12	10·56	10·32	10·44	10·40
MgO	5·23	5·05	5·23	5·11	4·73	5·17	5·07	5·13	5·06
MnO	0·17	0·17	0·17	0·17	0·17	0·17	0·17	0·17	0·19
K_2O	1·45	1·46	1·41	1·47	1·57	1·46	1·52	1·49	1·32
Na_2O	3·67	3·72	3·64	3·68	3·84	3·70	3·71	3·71	2·77
P_2O_5	0·50	0·51	0·50	0·51	0·54	0·52	0·53	0·52	0·51
Total	99·59	99·36	99·53	99·42	100·48	99·53	100·34	100·44	100·66
LOI	–0·29	–0·32	–0·15	–0·33	–0·32	0·12	0·03	–0·03	1·27
ppm									
Rb	36	35	30	33	34	33	32	36	27
Ba	768	773	701	712	737	782	713	780	764
Th	33	33	27	27	28	34	29	34	39
U	<20	<20	<20	<20	<20	<20	<20	<20	<20
Nb	50	53	47	46	49	53	51	54	59
La	75	87	87	66	79	81	80	86	80
Ce	135	123	118	132	126	131	133	131	138
Pb	30	22	19	17	20	20	21	20	18
Sr	1171	1183	1161	1169	1205	1166	1172	1178	1251
Nd	44	53	49	47	50	47	47	51	49
Zr	211	216	215	215	225	220	223	219	241
Y	27	27	25	23	25	28	25	28	31
Ni	31	33	32	30	30	31	34	47	34
Cr	52	48	57	47	40	47	44	67	43
V	253	259	245	227	238	260	252	261	292
Co	31	31	28	27	28	32	28	31	34
Cu	127	134	94	107	115	120	112	132	140
Zn	91	94	84	80	84	99	94	97	110

LOI, loss on ignition; it should be noted that the MtRs sample has a high LOI, which is not untypical for scoria.

studies on porphyritic mafic systems have highlighted that accumulation of early mineral phases plays a major role in whole-rock compositional variations (e.g. Sakyi *et al.*, 2012; Ubide *et al.*, 2012, 2014; Larrea *et al.*, 2013), such variations need to be evaluated in terms of differential accumulation of phenocryst phases.

To investigate this possibility, we present selected variation diagrams of bulk-rock data together with representative phenocryst compositions as Supplementary Data in Electronic Appendix 5, following the approach of Ubide *et al.* (2014). The anomalous composition of SET2 samples from Corsaro *et al.* (1996) (i.e. higher concentrations in SiO_2, Al_2O_3 and total alkalis and lower concentrations in FeO and TiO_2 than the other bulk-rock samples; Fig. 3) would agree with preferential accumulation of plagioclase phenocrysts relative to olivine or clinopyroxene phenocrysts. In addition, we find that our samples have higher contents of CaO (mean 10·51 wt % SET1 and 10·36 wt % SET2) and lower concentrations of MgO (mean 5·15 wt % SET1 and 5·02 wt % SET2) than the SET1 samples (Fig. 3f and g) studied by Corsaro *et al.* (1996). This could be related to preferential accumulation of clinopyroxene relative to olivine in our samples. Therefore, we interpret that the small geochemical variations observed between bulk-rock samples could be related to preferential accumulation of varied phenocryst phases. In other words, SET1 and SET2 lavas are probably composed of similar melts accumulating slightly varied phenocryst cargoes (Supplementary Data Electronic Appendix 6).

OLIVINE ZONING AND COMPOSITIONAL RECORD

Olivine zoning patterns

We studied a total of 202 olivine crystals ($n = 117$ SET1; $n = 68$ SET2; $n = 17$ MtRs) across the 11 samples studied; 198 (98%) of the studied olivine crystals were characterized by systematic normal (decreasing forsterite contents towards the rims) and to a minor extent (2%; i.e. four crystals) also reverse (increasing forsterite contents towards the rims) zoning patterns. These are classified by zoning type into the classification scheme employed by Kahl *et al.* (2015), who studied a total of 180 olivine crystals from recent (1991–2008) eruption products of Etna. The 1991–2008 olivines were characterized by multiple zoning patterns ranging from normal to reverse, or more complex zoning, with reversely zoned cores and normally zoned rims. Based on this large range of zoning patterns, Kahl *et al.* (2015) established eight zoning types (Type I–Type VIII). Extending that classification scheme to the 1669 olivines, we

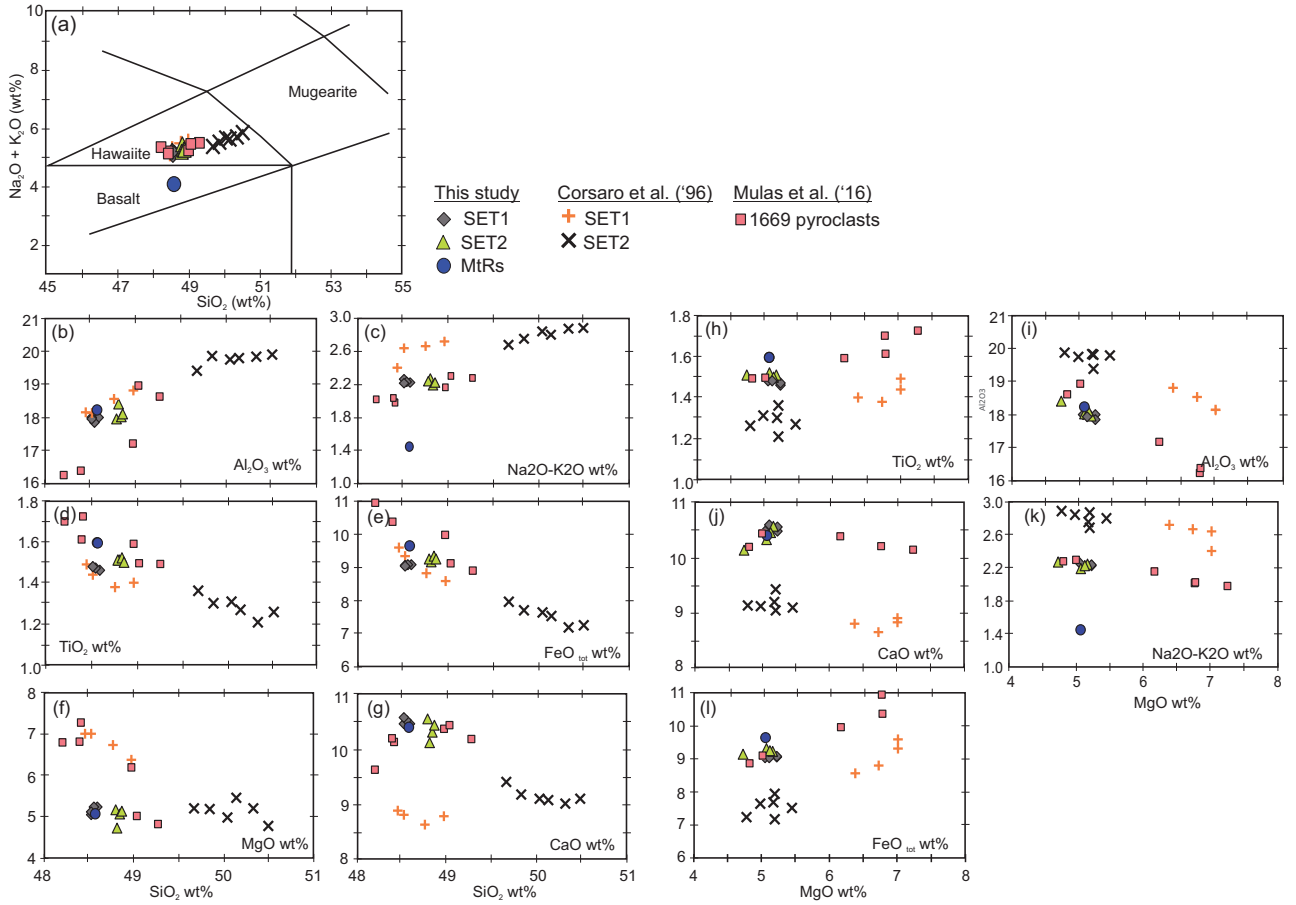

Fig. 3. (a) Total alkalis vs silica diagram (wt %) of 1669 samples studied by Corsaro *et al.* (1996) and from this study (filled diamonds, SET1; triangles, SET2; circle, MtRs). (b–l) Major element concentrations of whole-rocks of SET1, SET2 and MtRs samples from this study and of Corsaro *et al.* (1996).

observe that the zoning patterns preserved in the 1669 olivines consist predominantly of simple single-step normal or reverse zonations. This finding contrasts with the diversity of olivine zoning patterns identified in the recent 1991–2008 eruption products. From the eight zoning types (Type I–Type VIII) described by Kahl *et al.* (2015), six could be recognized in the 1669 olivines. Of those, Types IV and VII (Fig. 4) are the most abundant (186 crystals out of 202), as follows.

Type IV. This represents normally zoned crystals with intermediate core compositions of $Fo_{75–78}$ followed by low-forsterite rims (~Fo_{55} for SET1; ~Fo_{70} for SET2 and MtRs; Fig. 4a). This zoning type is by far the most abundant observed in the 1669 samples. It is identified in 71% (i.e. 144 crystals) of the studied olivines and can be found in all samples.

Type VII. This describes normally zoned crystals (21%; i.e. 42 crystals) with cores of $Fo_{73–75}$ and variable rim compositions (~Fo_{55} SET1 and ~Fo_{70} SET2; Fig. 4b). Together with type IV this zoning type occurs frequently in the SET1 and SET2 olivines. In the MtRs bomb sample, type VII could not be identified.

Besides these two dominant groups, minor zoning types (16 out of 202 crystals) have been identified (see Supplementary Data Electronic Appendix 7), as follows.

Type I: reversely zoned crystals with low-forsterite ($Fo_{70–72}$) cores and rim compositions at Fo_{75}.

Type II: normally zoned olivines with high-forsterite cores ($Fo_{79–83}$) and rims of variable composition ($Fo_{70–71}$ for SET2).

Type VI: crystals consisting of weak reverse zoning with intermediate core compositions ($Fo_{73–75}$) followed by subtle increase of the forsterite content towards the rims (~Fo_{75}) and reverse zoning with decreasing forsterite values at the outermost rims (Fo_{72}). The occurrence of this zoning type is limited to the Monte Rossi bomb sample.

Type VIII: normally zoned crystals with low-forsterite core composition of $Fo_{70–72}$ and rim compositions as low as Fo_{55}. This type is limited to SET1 eruption products.

Olivine compositional record

Besides variable zonation sense and pattern, the 1669 olivine crystals differ in terms of their specific core and rim compositions; the observed olivine compositions vary over a considerable range from Fo_{51} to Fo_{83}. In Fig. 5a and b frequency histograms illustrate the distribution of core and rim compositions of the 202 olivine crystals

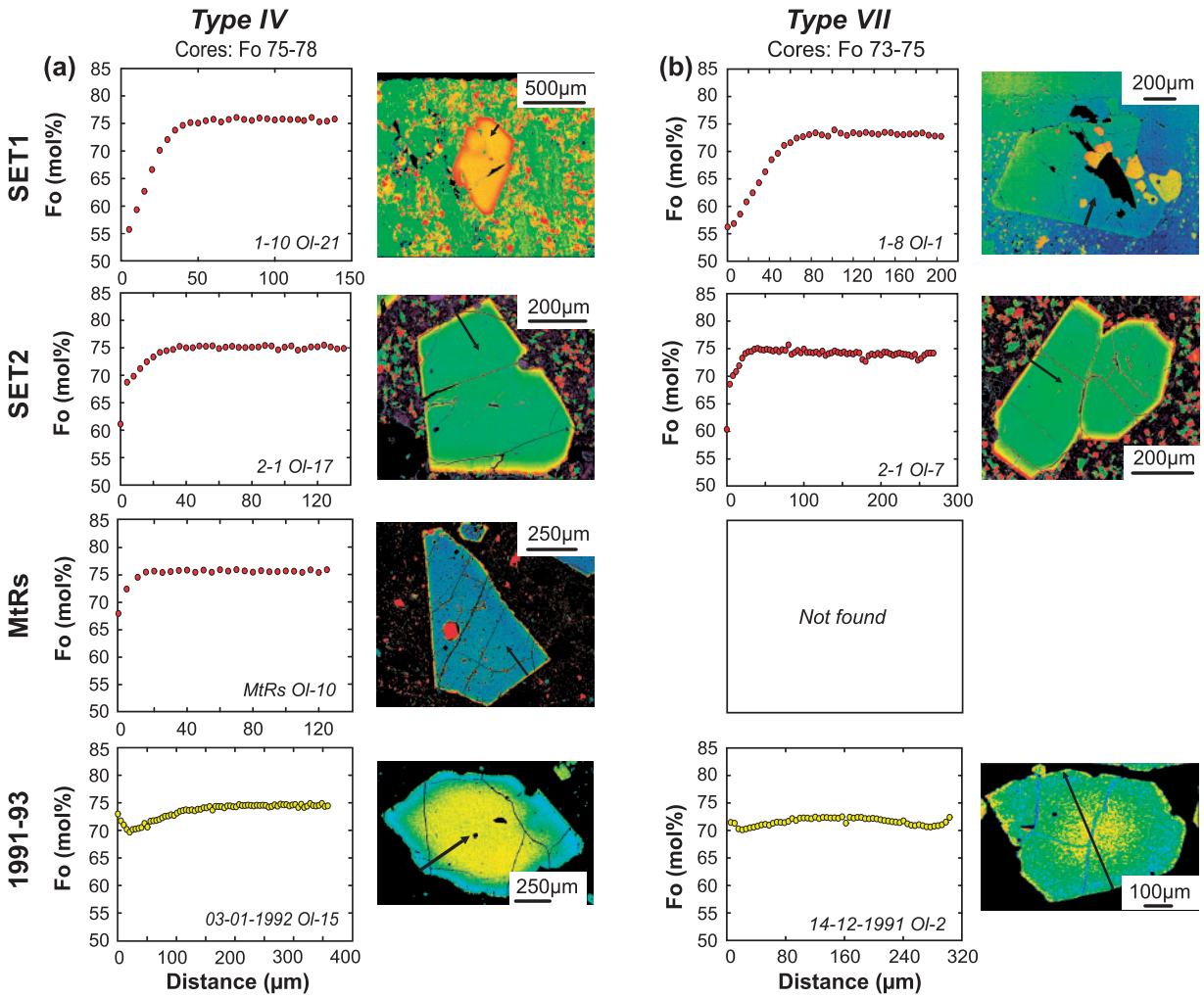

Fig. 4. Illustration of the most common zoning types identified in the 1669 olivine crystals. Columns: rim to core and rim to rim zoning profiles; arrows in BSE images display direction of electron microprobe traverse. Rows: zoning types as functions of eruption phases: SET1, SET2 and MtRs. Bottom row displays complexities of the different zoning types as identified in 1991–1993 samples (Kahl *et al.*, 2015). Fo, forsterite; Fo = 100 Mg/(Mg + Fe). (a) Type IV, normally zoned crystals with cores at $Fo_{75–78}$ and rims at ~Fo_{55} (SET1) or ~Fo_{70} (SET2 and MtRs). (b) Type VII, normal zoning with core at $Fo_{73–75}$ and variable rims. 'Not found' indicates that a particular zoning type could not be identified in the corresponding eruption product(s).

studied. All olivine data are provided in Supplementary Data Electronic Appendix 8.

The observed core compositions display a narrow compositional spectrum ranging from Fo_{71} to Fo_{83} with a dominant peak at Fo_{75} (Fig. 5a). The rim compositions, however, show a much broader compositional range from Fo_{51} to Fo78 (Fig. 5b). Overlap between the SET1 and SET2–MtRs does occur but is minor, affecting ~6% of the crystals (i.e. 13 crystals), which have definably different compositional modes. We observe different modes in the rim compositional record of the SET1, SET2 and MtRs olivines. SET1 olivine rims display compositions ranging between Fo_{51} and Fo_{65}, whereas the SET2 and MtRs rims vary between Fo_{64} and Fo_{77}, with a peak at Fo_{69} (Fig. 5b). This will be discussed in more detail in the following section.

In Fig. 5c–h minor element (MnO and CaO) plots of olivine core and rim compositions are shown. The olivine cores and rims show a negative correlation between forsterite and MnO content (Fig. 5c and d). The MnO contents of the olivine cores range between ~0·3 wt % for $Fo_{80–83}$ and 0·7 wt % for Fo_{71}. The rims have MnO contents ranging from 0·4 wt % for Fo_{75} (SET2 and MtRs samples) to ~1·35 wt % for Fo_{51} (SET1 samples).

The CaO contents of the olivine cores and rims are less variable, and range between 0·2 and 0·4 wt % for the cores (Fig. 5e) and between 0·3 and ~0·6 wt % (Fig. 5f) for the rims. Combining the CaO and MnO data, we find that the SET1 and SET2–MtRs olivines differ not only in their forsterite contents but also in their minor element chemistry (Fig. 5g and h), defining distinct fields. SET1 olivine rims are characterized by higher MnO and CaO contents than SET2 and MtRs rims. We take this as evidence that the olivine rims of SET1 and SET2 formed within compositionally different MEs that controlled both the major and minor element chemistries. In contrast, SET1 and SET2 olivine cores formed within the same ME.

Comparison with olivine compositions from recent (1991–2008) eruptions of Mt Etna

For comparison, we have added in Fig. 5a–f the compositional range of the five MEs identified in populations of zoned olivines erupted between 1991 and 2008 from Etna volcano (Kahl *et al.*, 2015). We find that the core compositional record of the 1669 olivines plots within the range of known olivine compositions (i.e. $Fo_{65–83}$) from recent and historical Etna eruptions (e.g. Clocchiatti & Métrich, 1984; Tanguy & Clocchiatti, 1984; Chester *et al.*, 1985; Métrich & Clocchiatti, 1989; Corsaro *et al.*, 1996, 2009; Spilliaert *et al.*, 2006; Kahl *et al.*, 2015). The most dominant core population—which can be tracked throughout all 1669 eruption products—is $Fo_{75–78}$ (144 crystals) followed by minor populations at $Fo_{73–75}$ (45 crystals), $Fo_{70–72}$ (10 crystals) and $Fo_{79–83}$ (three crystals). We observe that the two prominent olivine core populations in the 1669 products fall within the compositional range of the known MEs M_1 (= $Fo_{75–78}$) and mm_1 (= $Fo_{73–75}$; Fig. 5).

Regarding rim compositions, we observe two clearly distinct groups in the 1669 olivine dataset, as follows.

SET2 and MtRs. The rim compositional record of the SET2 and MtRs olivines displays two dominant populations at $Fo_{65–69}$ (49 crystals) and $Fo_{70–72}$ (30 crystals) and falls within the range of known MEs M_3 (= $Fo_{65–69}$) and M_2 (= $Fo_{70–72}$) described by Kahl *et al.* (2015). Minor populations can be observed at $Fo_{73–75}$ (four crystals) and $Fo_{75–78}$ (two crystals) and resemble the MEs defined by the olivine cores [i.e. M_1 (= $Fo_{75–78}$) and mm_1 (= $Fo_{73–75}$)].

SET1. The SET1 olivine rim compositions define a new compositional trend undetected in the recent

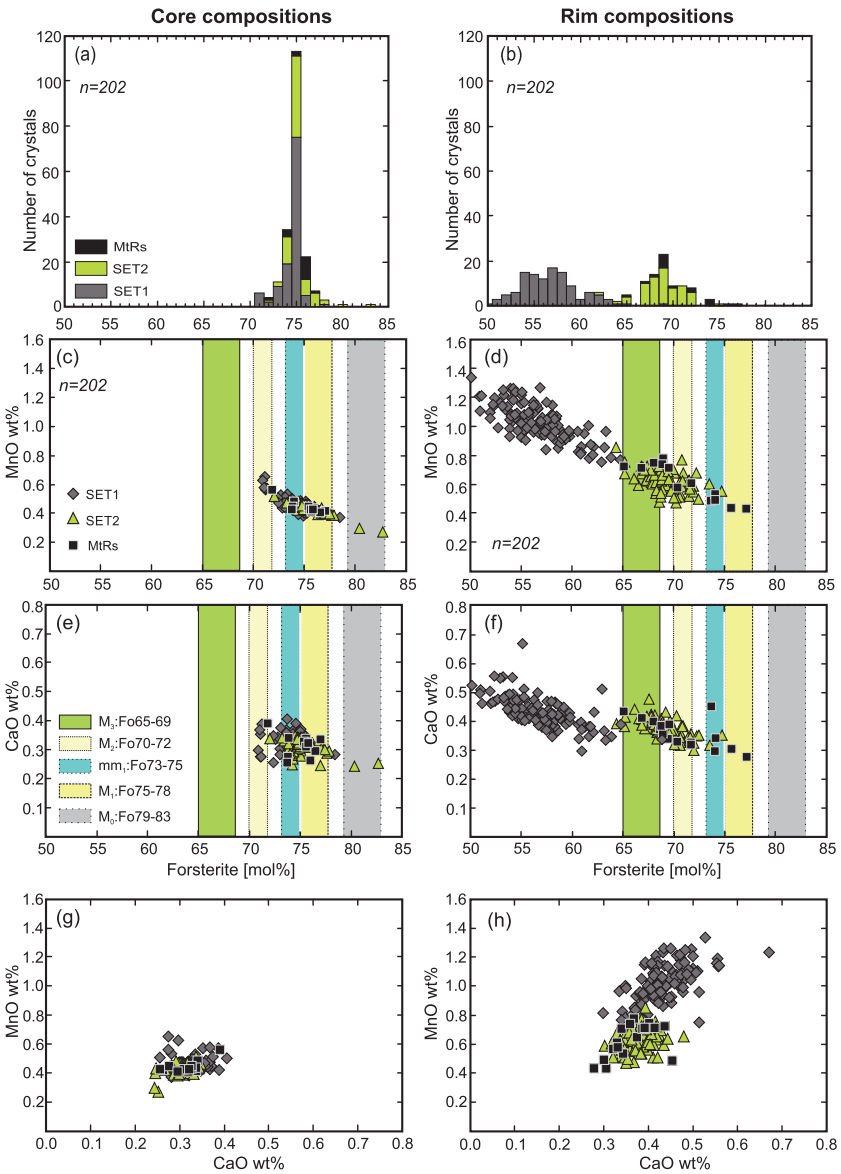

Fig. 5. (a, b) Frequency histograms of core and rim compositions of 202 olivine crystals erupted during the 1669 flank eruption. (c, d) MnO vs frsterite content of olivine cores and rims. (e, f) CaO vs forsterite content of olivine cores and rims. (g, h) MnO vs CaO plots of core and rim compositions. Coloured areas indicate compositional range of the five olivine populations identified in the 1991–2008 eruption products (Kahl *et al.*, 2015). Fo, Forsterite, Fo = 100 Mg/(Mg + Fe).

eruption products. SET1 rim compositions can be roughly subdivided into two populations, one at $Fo_{60–65}$ (17 crystals) and a second, bimodal population between Fo_{51} and Fo_{59} (99 crystals) with subtle peaks at Fo_{54} and Fo_{57}, respectively (Fig. 5b). From the minor element plots we can observe that both populations clearly differ from others in their higher MnO and CaO contents (Fig. 5d and f). We infer therefore that SET1 olivine rims formed in an ME distinct from those seen in recent products, which we define here as M_5.

Olivine trace element mapping

LA-ICP-MS element maps were obtained for selected olivine crystals Ol-5 (Type IV), Ol-12 (Type IV) and Ol-21 (Type IV) from sample 1-6 (SET1 lavas), Ol-1 (Type IV) and Ol-4 (Type IV) from sample 2-4 (SET2 lavas), and Ol-4 (Type IV) and Ol-6 (Type VI) from the MtRs bomb. Representative maps for minor and trace elements are presented in Fig. 6.

Olivine crystals show homogeneous cores and normally zoned rims. Concentrations in Mg and Ni decrease from the core to the rim of the crystals, and concentrations in Fe, Mn and Ca increase correspondingly. Such compositional change is observed in all analysed crystals, supporting the EMP results. In addition, LA-ICP-MS maps show that core–rim zoning is sharper in SET1 olivines, which show thicker, better developed rims than SET2–MtRs olivines (Fig. 6). Concentrations in V, Cr, Al, P, Sc and Ti are largely

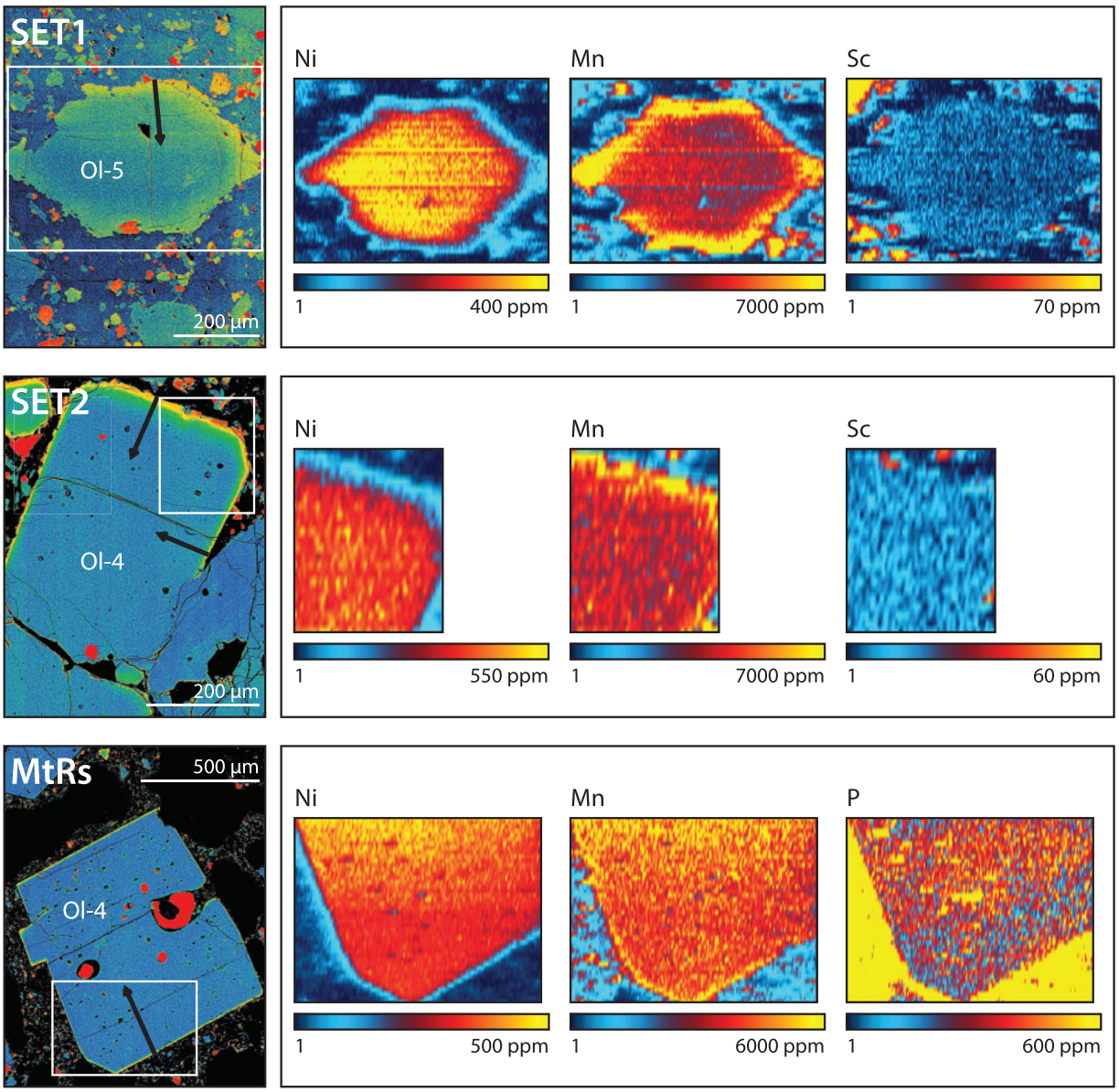

Fig. 6. LA-ICP-MS element maps for Ni, Mn, Sc and P in representative olivine crystals from SET1, SET2 and MtRs samples. Mapped areas are marked with white rectangles on false colour BSE images (black arrows indicate the direction of the electron microprobe traverses). LA-ICP-MS maps are constructed with the lolite module 'Images from integrations' using 'Cold–Warm' colour scales.

homogeneous across all olivine crystals and no zoning has been detected for these elements.

In summary, the detailed investigation of major, minor and trace element zoning profiles in 202 olivines reveals the existence of distinct compositional zonation (typically normal zonation) throughout all eruption products studied (SET1, SET2 and MtRs). This observation contrasts with the finding of Corsaro *et al.* (1996), in which a lack of compositional zoning in olivine phenocrysts (cores: $Fo_{73–77}$; rims: $Fo_{73–74}$) was reported, suggesting a sub-solidus homogenization owing to diffusive relaxation. An interesting observation arising from this study that has not been reported so far is the compositional variability and difference between the SET1 and SET2–MtRs olivine rims indicating that the olivine crystals (and their melts) experienced distinct and different late-stage magmatic histories following the formation of the cores. Although the SET1 and SET2 samples investigated in this study are rather similar in whole-rock composition, we find that *in situ* compositional information locked in the chemical stratigraphy of zoned olivine crystals reveals significant differences between the SET1 and SET2–MtRs samples.

UNRAVELLING THE ZONING RECORD

As outlined by Kahl *et al.* (2011, 2015), a characteristic that all identified olivine populations have in common is the existence of so-called compositional plateaux: zones or regions within a crystal characterized by constant forsterite values (Fig. 4; Supplementary Data Electronic Appendix 7). The occurrence of these plateaux was attributed to the stepwise growth of the crystals within different MEs, which in turn may be characterized by a different set of thermodynamic parameters (e.g. temperature, pressure, oxygen fugacity, water content and melt composition). To produce extended plateaux of constant forsterite contents the ambient parameters must have been kept constant during growth, otherwise continuous variations in the compositional profiles (as observed during cooling or fractionation), rather than plateaux with sudden jumps, would be expected (Kahl *et al.*, 2015).

We make use of the method outlined by Kahl *et al.* (2011) to illustrate the comprehensive zoning record preserved in the studied olivine crystals in systems analysis diagrams (Fig. 7). To improve the clarity of these diagrams we discarded connection lines that are recorded by fewer than two crystals from each of the systems analysis plots (Fig. 7). A total of six crystals (one from SET1, two from SET2 and three from MtRs) were affected by these reductions. We found eight crystals that are homogeneous ($Fo_{75–78}$) without compositional zoning and are therefore also not displayed in the systems analysis plots. This explains why the number of connection lines (and therefore crystals) shown in Fig. 7 (i.e. 188) is less than the total number of crystals (i.e. 202) analysed.

We could identify six MEs that account for the compositional diversity observed in the 1669 olivines. Of these, two are so-called 'core environments' because the majority of the olivine cores have formed in them; that is, M_1 (= $Fo_{75–78}$) and mm_1 (= $Fo_{73–75}$). The other four are 'rim environments' in which the SET1 and SET2–MtRs olivine rims crystallized; that is, M_2 (= Fo70–72), M_3 (= $Fo_{65–69}$), M_4 (= $Fo_{60–65}$) and M_5 (= $Fo_{50–59}$). Of these, M_3 and M_5 are dominant.

The thickness of the connection lines shown in Fig. 7a–c is directly linked to the number of crystals tracking a certain connectivity path (i.e. connection between two MEs). The majority of the MEs such as M_1 (= $Fo_{75–78}$), M_2 (= $Fo_{70–72}$) and mm_1 (= $Fo_{73–75}$) were

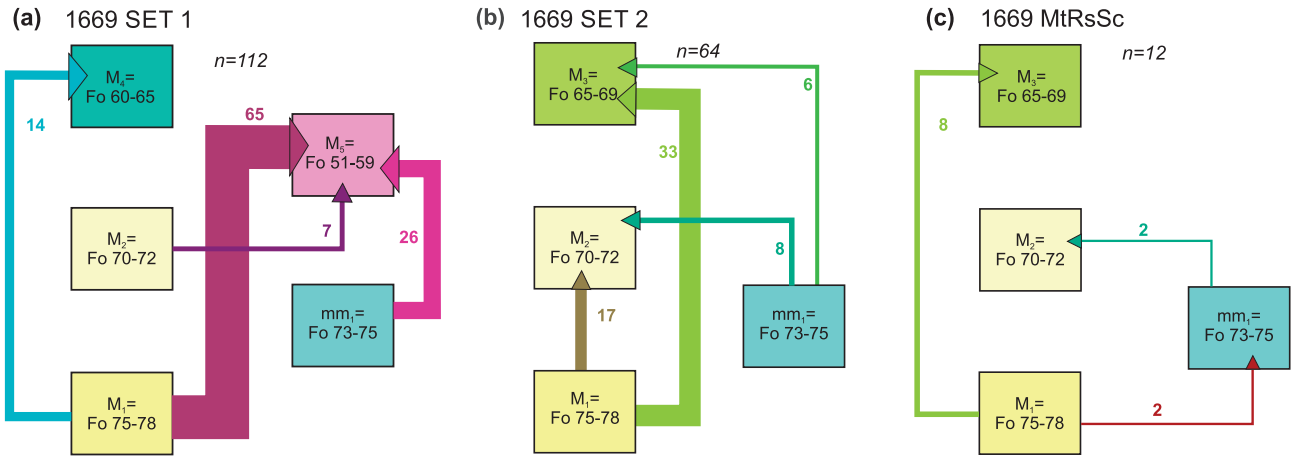

Fig. 7. Individual systems analysis diagrams of zoning patterns recorded in a total of 188 olivine crystals contained in the SET1 (a), SET2 (b) and MtRs (c) samples of the 1669 eruption. The number of olivine zoning patterns depicted in the systems analysis plots is smaller than the total number of crystals investigated ($n = 202$). Minor connection lines recorded by only one crystal have been removed to improve visibility. Each coloured box represents a different Magmatic Environment (ME) as identified based on the six olivine core and rim populations. Connection lines between these MEs represent zoning patterns recorded in populations of olivine crystals. The variable thickness of the connection lines refers to the number of crystals tracking certain connectivities. The corresponding numbers are given next to each connection line. The arrows indicate the direction of the zoning patterns as recorded in the olivine crystals (arrowheads point in the direction of olivine rims).

already identified in the 1991–2008 olivines, where it was found that these MEs are well connected in the 'modern' plumbing system of Etna (Kahl *et al.*, 2015). On the other hand, more evolved environments such as M_3 (= $Fo_{65–69}$) were only occasionally identified in the 1991–2008 samples. In fact, the only recent samples possessing a dominant population of olivines recording a highly evolved environment M_3 (= $Fo_{65–69}$) were those related to paroxysms (e.g. April 11, May 7 and September 9) of the 2007 summit activity. Given the scarcity of examples, the M_3 environment was previously believed to represent a transient, rarely sampled feature of the plumbing system (Kahl *et al.*, 2015). The 1669 products, in contrast, present abundant evidence (i.e. rim compositions of olivines; Fig. 5) that MEs containing highly evolved magmas such as M_3 (= $Fo_{65–69}$), M_4 (= $Fo_{60–65}$) and M_5 (= $Fo_{50–59}$) could have played a major role in historical eruptions at Mt Etna and are likely to represent long-term features of Etna's historical plumbing system. Highly evolved environments such as M_4 (= $Fo_{60–65}$) and M_5 (= $Fo_{50–59}$) have not been shown to be involved in modern activity (Viccaro *et al.*, 2015; M. Pompilio, personal communication), implying that significant changes have occurred over historical time.

Below, we describe the connection history observed through the systems analysis of the 1669 eruption products and we discuss how connectivities change over time.

1669 SET1. In the SET1 olivines we observe mainly two dominant connection patterns (Fig. 7a), interlinking the 'core environments' M_1 (= $Fo_{75–78}$) and mm_1 (= $Fo_{73–75}$) with the highly evolved 'rim environment' M_5 (= $Fo_{51–59}$). Besides the main connection routes M_1–M_5 (65 crystals) and mm_1–M_5 (23 crystals), there are minor routes connecting the environments M_1–M_4 (14 connections) and M_2–M_5 (seven connections).

1669 SET2. The SET2 olivines also display two dominant populations (Fig. 7b) tracking the connections M_1–M_3 (33 crystals) and M_1–M_2 (17 crystals). A few crystals record the histories mm_1–M_2 (8 crystals) and mm_1–M_3 (6 crystals).

1669 MtRs. In this sample we find olivines that record fewer connections. We observe one population (8 crystals) that tracks the connection M_1–M_3 (Fig. 7c). Minor connections are related to the environments

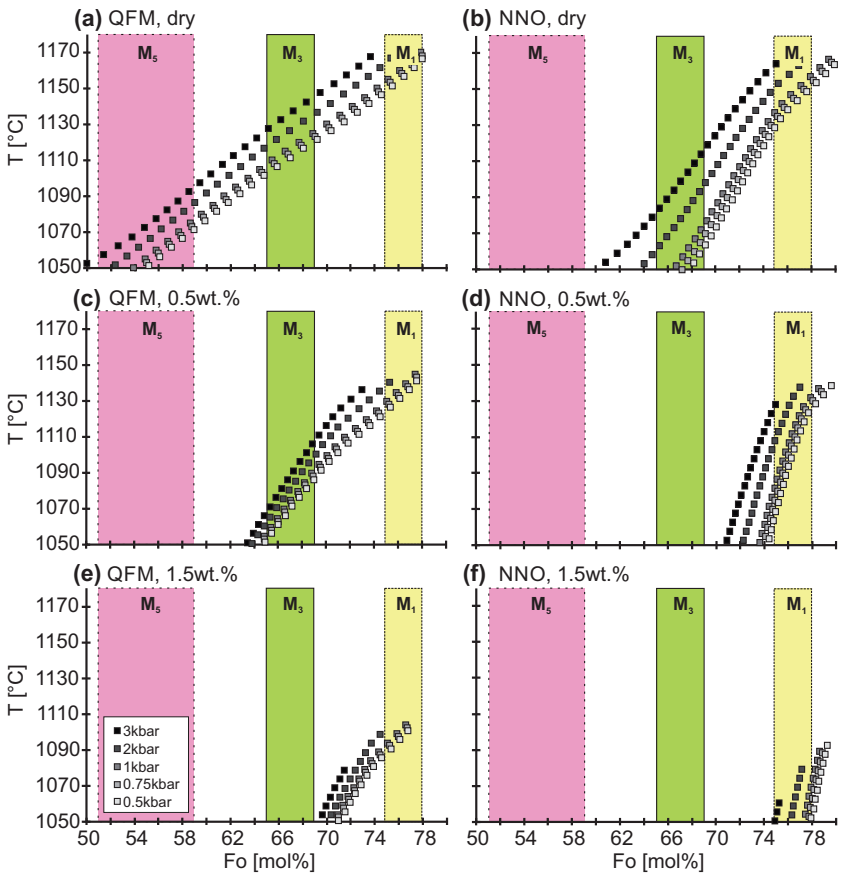

Fig. 8. Olivine compositions (Fo mol %) obtained from fractional crystallization (FC) simulations using rhyolite-MELTS (Gualda *et al.*, 2012; Ghiorso & Gualda, 2015). The simulations were performed using the bulk-rock compositions shown in Table 3 at the quartz–fayalite–magnetite (QFM) and the Ni–NiO (NNO) oxygen buffers, and variable water contents (dry to 1·5 wt % water). Vertical axis: crystallization temperature in degrees Celsius; horizontal axis: forsterite content. Filled squares, olivine compositions obtained for a given isobaric cooling path. M_1, M_3 and M_5, compositional range of olivine core and rim populations characterizing the dominant 'core' [i.e. M_1 (= $Fo_{75–78}$)] and 'rim forming' [i.e. M_3 (= $Fo_{65–69}$) and M_5 (= $Fo_{51–59}$)] environments.

mm_1–M_2 (2 crystals) and M_1–mm_1 (2 crystals). The connection patterns in the MtRs olivines show a close resemblance to those found in the SET2 olivines (Fig. 7c), suggesting that the crystals contained in the MtRs and the SET2 magmas experienced the same late-stage magmatic history.

In summary, from the combined systems analysis record of the 1669 samples, we find that the vast majority (96%) of the olivine cores record a common early stage magmatic history related to crystal growth or residence in the MEs M_1 (= $Fo_{75–78}$; i.e. 139 crystals) and mm_1 (= $Fo_{73–75}$; i.e. 42 crystals). The identification of four 'rim environments' [i.e. M_5 (= $Fo_{50–59}$; 98 crystals), M_4 (= $Fo_{60–65}$; 14 crystals), M_3 (= $Fo_{65–69}$; 47 crystals) and M_2 (= $Fo_{70–72}$; 27 crystals)] suggests diverging late-stage magmatic histories in SET1 vs SET2–MtRs samples, following the formation of the olivine cores in the dominant environment M_1.

CHEMICAL AND PHYSICAL CHARACTERISTICS OF MAGMA STORAGE

We applied thermodynamic calculations using the rhyolite-MELTS software (Gualda *et al.*, 2012; Ghiorso & Gualda, 2015) to characterize the MEs in which the cores and the different rims of the SET1 and SET2–MtRs olivines formed.

Following the modelling procedure outlined by Kahl *et al.* (2015), we started with the identification of appropriate starting compositions (glass or whole-rock) from which the most primitive olivine composition observed [i.e. M_1 (= $Fo_{75–78}$)] could have crystallized. The bulk composition of the magma provides the largest source of variability. Therefore, we checked carefully the given range of bulk compositions (Table 3) for the SET1, SET2 and MtRs samples. We find that each of these compositions could be in equilibrium with the most primitive olivine population ($Fo_{75–78}$) identified in the 1669 Etna eruption products.

In addition to major element chemistry, water contents and the prevalent oxygen fugacity conditions (fO_2) can have a significant impact on crystallization paths (e.g. Kahl *et al.*, 2015). Micro-analytical studies of olivine-hosted melt inclusions (MIs) in the 1669 eruption products reveal variable, but low, total water contents (1·0–0·3 wt %; e.g. Clocchiatti & Métrich, 1984; Métrich & Rutherford, 1998). The oxidation state of Etna lavas has been constrained by the type of Fe–Ti oxides present (e.g. Métrich & Clocchiatti, 1996; Kahl *et al.*, 2011), as well as through experimental studies (e.g. Pompilio & Rutherford, 2002), to lie in the vicinity of the Ni–NiO reaction (NNO) oxygen fugacity buffer.

The forward modelling strategy using the rhyolite-MELTS software (Gualda *et al.*, 2012; Ghiorso & Gualda, 2015) was defined as follows. We started with the melt compositions provided in Table 3 simulating fractional crystallization, following the demonstration by Kahl *et al.* (2015) that equilibrium crystallization cannot explain observed compositional diversity in modern Etna samples. Fractional crystallization was modelled along different fO_2 paths (QFM or NNO) for different initial water contents (1·5 wt % to dry). Finally, the *P–T* space was scanned along isobaric lines (3·0–0·5 kbar) at a temperature range starting from liquidus down to 1050°C, in agreement with the lowest temperatures obtained by geothermometry (1070 ± 20°C; 1081 ± 17°C; Kahl *et al.*, 2015), applying the geothermometer of Loucks (1996), at intervals of 5°C. The sets of conditions at which olivines corresponding to the different MEs could have formed are shown in Fig. 8 and the results of the MELTS simulations are summarized in Supplementary Data Electronic Appendix 9. The applied conditions were considered plausible for a given ME only when the full compositional range of olivine corresponding to that ME (e.g. $Fo_{75–78}$ for M_1) could be obtained.

At melt water contents ranging from dry to 1·1 wt %, olivine compositions corresponding to the ME M_1 can be obtained at QFM or NNO, temperatures between 1060 and 1170°C and pressures ≤1 kbar (Fig. 8a–d). M_1 olivines typically coexist with clinopyroxene, plagioclase and Fe–Ti oxides with compositions that lie within the observed range of natural compositions ($An_{56–85}$, Corsaro *et al.*, 1996; Mg# 73–93 and $Mt_{35–52}$, this study). At QFM, the obtained clinopyroxene compositions (i.e. Mg# 81–83) match the mafic end of the observed natural compositions whereas the modelled plagioclase compositions (i.e. $An_{66–75}$) fall within the intermediate range of observed natural compositions. The simulated Fe–Ti oxide compositions (i.e. $Mt_{35–38}$) match the lower end of natural compositions. At NNO, the results are similar, with the distinction that the obtained Fe–Ti oxide compositions (i.e. $Mt_{50–57}$) fall outside the compositional range of observed Fe–Ti oxides.

These observations are in agreement with the results presented by Kahl *et al.* (2015). Those researchers found that M_1 olivines form at QFM or NNO, temperatures ≥1110°C and melt water contents between 0·1 and 1·4 wt % coexisting with clinopyroxene (Mg# 80–85), plagioclase ($An_{50–83}$) and Fe–Ti oxides ($Mt_{45–58}$), using a bulk-rock composition of the 2002–2003 south-flank eruption of Mt Etna (MgO content 8·17 wt %) as the starting composition. M_1-type olivines coexisting with An-rich ($An_{80–83}$) plagioclase at QFM or NNO and low melt water contents could be reproduced only at low pressures between 0·25 and 0·75 kbar. The only distinction in the results obtained in the present study is that M_1 olivines and Fe–Ti oxides could coexist only at oxygen fugacity conditions buffered at NNO (Kahl *et al.*, 2015).

Evolved olivine compositions corresponding to M_3 (= $Fo_{65–69}$) can be reproduced primarily under QFM conditions and lower temperatures (below 1140°C). M_3 olivines form at melt water contents ranging from dry to 1·3 wt % at all pressures considered (0·5– 3·0 kbar) (Fig. 8a and c) together with clinopyroxene (Mg# 74·5–78·4), plagioclase ($An_{53–64}$) and Fe–Ti oxides ($Mt_{43–52}$). At NNO, M_3 olivines form at high pressures (i.e. 2·0–3·0 kbar; Fig. 8b) and dry conditions only, together with clinopyroxene (Mg# 74–79). Kahl *et al.* (2015) were able to reproduce M_3 olivines at QFM, low melt water contents

(0·2–0·4 wt %), temperatures below 1100°C and all pressures considered (0·5–3·0 kbar) together with clinopyroxene, plagioclase and Fe–Ti oxides with the observed compositions.

The most evolved olivine compositions M_5 (= $Fo_{51–59}$) identified in the 1669 samples form at QFM only, under dry conditions, temperatures below 1100°C and pressures between 1·0 and 3·0 kbar (Fig. 8a). At these conditions only clinopyroxene (Mg# 74) forms with the observed compositions. Olivines of this composition could not be reproduced in the study of Kahl *et al.* (2015).

From our MELTS simulations we find that plagioclase is the liquidus phase of the 1669 magmas at all pressures and water contents considered. We observe that An-rich plagioclase compositions (i.e. $An_{80–85}$) are not in equilibrium with any of the observed olivine populations and can form at pressures from 0·5 to 3·0 kbar, melt water contents of 1·5 and 2·5 wt % (the latter for An_{85}) and temperatures between 1090 and 1144°C, irrespective of the oxygen fugacity conditions. The bulk of the more evolved plagioclase compositions (i.e. $An_{53–75}$), however, form in equilibrium with the observed olivine populations ($An_{53–64}$ with M_3; $An_{66–75}$ with M_1) but at lower melt water contents (dry to 1·3 wt %). The most evolved olivine population M_5 does not coexist with plagioclase compositions in the observed range. We believe that the lower water contents, at which the bulk of the evolved plagioclase crystals form in equilibrium with the majority of the observed olivine and evolved clinopyroxene compositions, could be related to shallower depths reached by SET1 and SET2 magmas ($P < 800$ bar; e.g. Métrich & Rutherford, 1998). In summary, the observed differences in the MEs the olivines and their melts passed through are mainly related to changes in the melt water content, oxygen fugacity and temperature.

TIME-INTEGRATED APPROACH—DIFFUSION MODELLING

Following the approach outlined by Kahl *et al.* (2011, 2013) we have modelled the diffusive relaxation of compositional zoning profiles in 150 olivines from the SET1 and SET2 samples. The criteria for the choice of concentration profiles for modelling and tests for robustness have been reported in full detail by, for example, Costa *et al.* (2008) and Kahl *et al.* (2011, 2013). We note that the compositional zoning profiles preserved in olivines from the Monte Rossi (MtRs) bomb sample were not robust enough (i.e. weak zoning) for diffusion modelling and these crystals were therefore discarded. The application of diffusion modelling to the identified olivine populations allows us to (1) assess the timing and duration over which the crystals (plus their associated melts) have been transferred between the MEs identified and (2) reconstruct the residence times of the SET1 and SET2 magmas within different sections of the plumbing system prior to eruption.

Modelling approach

For our modelling approach, we made use of the following one-dimensional expression of the diffusion equation (i.e. Fick's second law):

$$\frac{\partial C_i(x,t)}{\partial t} = \frac{\partial}{\partial t}\left[D_i \frac{\partial C_i(x,t)}{\partial x}\right] \quad (1)$$

where C_i is the concentration of element i, x denotes the distance, D_i is the diffusion coefficient of element i, and t is time. The evolution of the concentration with time (t) at different spatial coordinates (x), $C_i(x,t)$, is obtained numerically using a one-dimensional finite difference scheme. An example diffusion Mathematica code is provided as Supplementary Data (Electronic Appendix 9) of Kahl *et al.* (2015) and can also be obtained from the authors. In this study, we focused predominantly on Fe–Mg zoning in olivine, using Fe–Mg diffusion coefficients obtained by Dohman & Chakraborty (2007) and Dohmen *et al.* (2007). Minor (Mn, Ca, Ni) and trace element (Al, P, Ti, Cr) profiles were obtained and carefully checked using EMP analysis and high-resolution LA-ICP-MS mapping (Ubide *et al.*, 2015; Fig. 6), but did not yield characteristic zoning patterns that could be used for diffusion modelling.

As diffusion of most elements in olivine is strongly orientation dependent with respect to the crystal lattice, we have taken into account the effects of diffusion anisotropy. For this purpose, the orientation and the angular relation of the crystallographic *a*-, *b*- and *c*-axes in the analysed olivine crystals were determined using EBSD (see Analytical Methods for further details).

Input parameters—temperature and oxygen fugacity (fO_2)

Magmatic temperatures were determined using the Fe–Mg exchange geothermometer between coexisting clinopyroxene and olivine rims (Loucks, 1996) and were 1070 ± 20°C. The oxygen fugacity (fO_2) conditions were set to QFM, given that at this temperature range, thermodynamic calculations using rhyolite-MELTS (Gualda *et al.*, 2012; Ghiorso & Gualda, 2015) indicate that M_3- and M_5-type olivine cannot be formed at NNO (Kahl *et al.*, 2015).

Examples of calculated diffusion models that fit the concentration profiles are shown in Fig. 9. Propagation of errors and uncertainties of the obtained timescales were determined following the procedure described by Kahl *et al.* (2015). A frequency distribution of all calculated timescales is shown in Fig. 10a.

Timescale results

Applying the procedures outlined above, we obtained 150 time estimates (SET1 = 109; SET2 = 41) from modelling the diffusive relaxation of Fe–Mg zoning profiles in 150 olivine crystals (Fig. 10a). A summary with all modelled timescales and the sequence of MEs as recorded in the chemical stratigraphy of the crystals is provided in Table 4. The observed distribution of timescales is

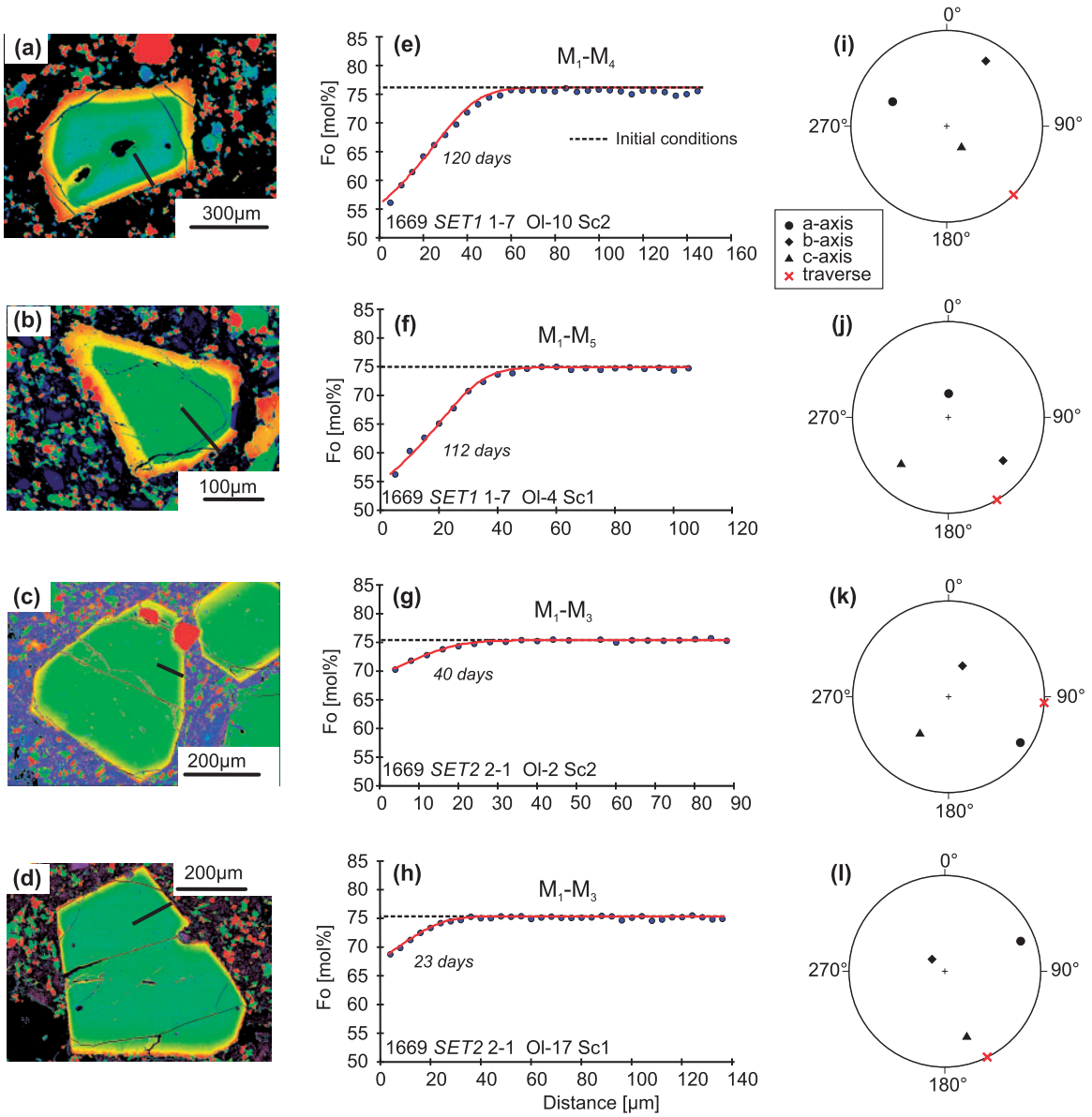

Fig. 9. Diffusion model fits. (a–d) False colour BSE images of representative olivine crystals. Black lines indicate directions of EMP traverses. (e–h) Core to rim concentration profiles of olivine crystals erupted during the 1669 flank eruption of Mt Etna. Blue circles, EMP traverses showing concentration profiles for forsterite [100Mg/(Mg + Fe), in mol %]. Black dashed lines, initial conditions; red lines, best-fit diffusion models for the observed zoning profiles. Numbers in days indicate diffusive timescales obtained from best-fit model solutions. M_1, M_3, M_4 and M_5 indicate core and rim formation within distinct Magmatic Environments. (i–l) Stereographic lower hemisphere plots depicting the angular relations between the major crystallographic directions (*a*-, *b*- and *c*-axes) in olivine and the directions of the analytical traverses. Olivine orientation data were obtained using the EBSD technique (see Analytical Methods section for full details).

fairly large, ranging from a minimum of a few days to a maximum of 1·5 years, with the majority (76%) of the obtained time estimates being shorter than 3 months (Fig. 10a). The observed array of timescales is in good agreement with results from recent Etna eruptions (e.g. Kahl *et al.*, 2011, 2013, 2015) and other basaltic volcanoes (e.g. Albert *et al.*, 2015; Hartley *et al.*, 2016; Rae *et al.*, 2016; Viccaro *et al.*, 2016*b*). Corresponding timescales of SET1 (red diamonds) and SET2 (green triangles) olivines are shown in Fig. 10b. The horizontal bars represent the associated 1σ errors related to uncertainties from geothermometry [see Kahl *et al.* (2015) for details on error propagation procedures].

1669 SET1. Time estimates related to the initial stages of the eruption (i.e. March 11–20, 1669) range from 16 days to 1·5 years with the majority (61%) being shorter than 3 months (Fig. 10b).

1669 SET2. Time estimates related to the second half (i.e. post-March 29, 1669) of the eruptive activity are shifted towards slightly shorter timescales (10 days to ~5 months) with the majority (71%) being shorter than 2 months (Fig. 10b).

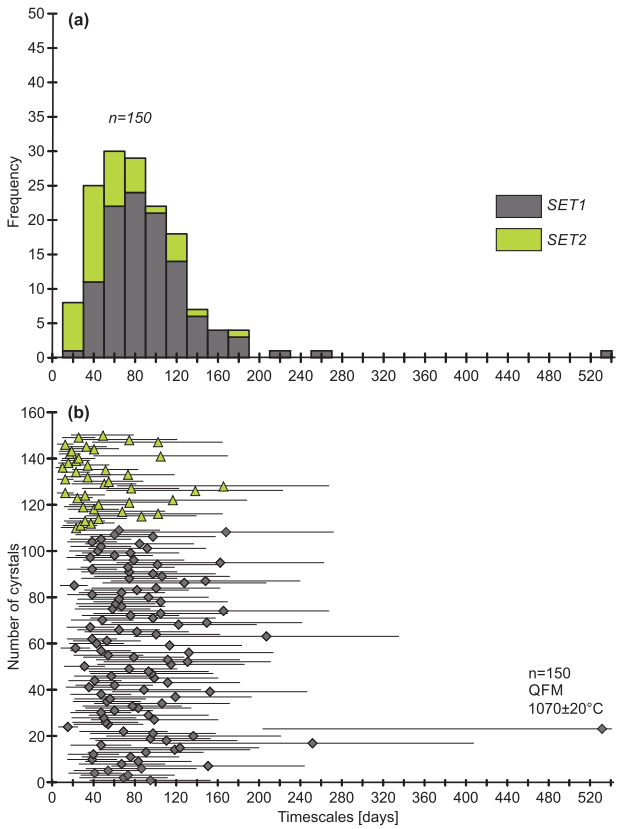

Fig. 10. Comprehensive timescale record obtained from modelling the diffusive modification of Fe–Mg concentration profiles preserved in a total of 150 olivine crystals that fulfilled the robustness criteria described by Costa *et al.* (2008) and Kahl *et al.* (2011). (a) Frequency distribution of timescales for SET1 (grey) and SET2 (green) olivine crystals. Bin size is 20 days. (b) Compilation of calculated timescales as a function of crystal number including 1σ uncertainties arising from geothermometry. Coloured symbols refer to mixing timescales obtained from modelling single SET1 (grey diamonds) and SET2 (green triangles) olivines. Modelling parameters: $T = 1070 \pm 20°C$ and fO_2 = QFM. Diffusion models performed in this study used the Fe–Mg inter-diffusion coefficients provided by Dohmen & Chakraborty (2007) and Dohmen *et al.* (2007). No diffusion timescales for MtRs olivines were obtained, as EMP profiles did not fulfil the robustness criteria.

Timing of magma transfer

Kahl *et al.* (2011, 2013, 2015) demonstrated that the application of systems analysis to populations of zoned olivine crystals can be used to uniquely link the compositional information preserved in the chemical stratigraphy of olivines with the transport dynamics of their associated melts. Extending this approach to the 1669 olivines allows us to decipher diverging magmatic histories in the SET1 and SET2–MtRs olivines related to different magma transfer pathways connecting the 'core' and the 'rim' MEs. To obtain an idea of the timing and duration of magma transfer between these environments we have plotted the frequency of intrusive events as functions of the various migration routes identified in the systems analysis in Fig. 11. The intrusion times have been recalculated by successively subtracting the modelled olivine timescales from the assumed eruption

Table 4: Comprehensive timescale record of SET1 and SET2 olivines

Olivine	Timescale (days)	1σ	Sequence of magmatic environments
Sample 1–6			
Ol-1	95	59	mm_1–M_5
Ol-3	69	43	M_1–M_5
Ol-4	73	45	M_1–M_5
Ol-19	42	26	mm_1–M_5
Ol-16	55	34	M_1–M_5
Ol-11	86	53	M_1–M_5
Ol-13	151	93	M_1–M_5
Ol-12b	68	42	M_1–M_4
Ol-14	84	52	mm_1–M_5
Ol-28	39	24	mm_1–M_5
Ol-27	76	47	M_1–M_5
Ol-24	40	25	M_1–M_5
Ol-30	91	56	M_1–M_4
Ol-6	119	73	M_1–M_5
Ol-8	124	76	mm_1–M_5
Ol-9	48	29	M_1–M_5
Ol-5	252	156	mm_1–M_5
Ol-29	111	68	M_1–M_4
Ol-22	95	59	mm_1–M_5
Ol-23	137	84	mm_1–M_5
Ol-25	98	60	M_1–M_5
Ol-31	69	43	M_1–M_5
Ol-7	531	328	M_1–M_5
Sample 1–7			
Ol-23	16	10	M_1–M_5
Ol-22	55	34	M_1–M_5
Ol-21	52	32	mm_1–M_5
Ol-20	99	61	M_1–M_4
Ol-19	50	31	M_1–M_4
Ol-18	94	58	M_1–M_5
Ol-16	48	29	M_1–M_4
Ol-17	60	37	M_1–M_5
Ol-15b	84	52	M_1–M_5
Ol-14	78	48	M_1–M_5
Ol-13	107	66	M_1–M_5
Ol-12	53	33	M_1–M_5
Ol-11	56	35	M_2–M_5
Ol-10	120	74	M_1–M_4
Ol-9a	48	29	M_1–M_5
Ol-8b	153	94	M_2–M_5
Ol-8a	89	55	M_2–M_5
Ol-7	36	22	M_1–M_4
Ol-6	60	37	M_1–M_5
Ol-4	112	69	M_1–M_5
Ol-3	42	26	M_2–M_5
Ol-2a	99	61	M_1–M_5
Ol-1	58	36	mm_1–M_5
Ol-24	96	60	M_1–M_5
Ol-25	94	58	M_1–M_5
Ol-2c	75	46	M_1–M_5
Ol-2d	32	20	M_1–M_4
Sample 1–8			
Ol-19	115	71	M_1–M_5
Ol-18	131	81	mm_1–M_5
Ol-17	112	69	M_1–M_5
Ol-16	79	49	M_0–M_5
Ol-15	55	34	mm_1–M_5
Ol-14	132	82	mm_1–M_5
Ol-13	48	29	M_1–M_5
Ol-11	23	14	M_1–M_5
Ol-12	114	70	M_1–M_5
Ol-10	43	27	M_1–M_5
O-l9	53	33	M_1–M_5
Ol-7	39	24	M_2–M_5
Ol-6	207	128	M_2–M_5
Ol-5	101	62	M_1–M_5
Ol-4	82	51	mm_1–M_5

(continued)

Table 4: (continued)

Olivine	Timescale (days)	1σ	Sequence of magmatic environments
Ol-3	65	40	M_1–M_5
Ol-2	37	23	mm_1–M_5
Ol-1	122	76	mm_1–M_5
Sample 1–9			
Ol-1	150	92	M_1–M_5
Ol-22	49	30	M_1–M_5
Ol-18	98	60	M_1–M_5
Ol-14	76	47	M_1–M_5
Ol-21	105	65	M_1–M_5
Ol-20	166	102	M_1–M_5
Ol-24	59	36	M_2–M_5
Ol-19	68	42	mm_1–M_5
Ol-17	62	38	M_1–M_5
Ol-8	105	65	M_1–M_4
Ol-12	65	40	M_1–M_4
Ol-7a	94	58	M_1–M_5
Ol-7b	39	39	M_1–M_4
Ol-4	68	68	M_1–M_5
Ol-6	82	82	mm_1–M_5
Ol-2	101	101	mm_1–M_5
Ol-10	22	22	M_1–M_4
Ol-11	128	128	M_1–M_4
Ol-16	148	148	M_1–M_4
Ol-5	75	75	M_2–M_5
Ol-7c	107	107	M_1–M_4
Sample 1–10			
Ol-21b	98	60	M_1–M_5
Ol-20a	75	46	M_1–M_5
Ol-20b	39	24	M_1–M_5
Ol-18	73	45	M_1–M_5
Ol-17	102	63	mm_1–M_5
Ol-15	163	100	M_1–M_5
Ol-14	79	49	M_1–M_5
Ol-13	37	23	M_1–M_5
Ol-11	60	37	M_1–M_5
Ol-10	76	47	M_1–M_5
Ol-9a	45	28	mm_1–M_5
Ol-8	92	57	M_1–M_5
Ol-6	48	29	mm_1–M_5
Ol-5a	85	52	M_1–M_5
Ol-4	39	24	M_1–M_5
Ol-2	48	29	mm_1–M_5
Ol-1a	98	60	M_1–M_5
Ol-1b	60	37	M_1–M_5
Ol-12	168	104	M_1–M_5
Ol-22	65	40	M_1–M_5
Sample 2–1			
Ol-17	23	14	M_1–M_3
Ol-15	27	17	M_1–M_3
Ol-8	37	23	M_1–M_3
Ol-7	32	20	mm_1–M_3
Ol-6a	45	28	M_1–M_3
Ol-5	86	53	mm_1–M_2
Ol-4	102	63	M_1–M_3
Ol-3	68	42	M_1–M_3
Ol-2	40	25	M_1–M_3
Ol-1	30	19	M_1–M_3
Sample 2–2			
Ol-15	45	28	M_1–M_3
Ol-12	75	46	mm_1–M_3
Ol-11	117	72	M_1–M_3
Ol-10	24	15	M_1–M_2
Ol-7	32	20	M_1–M_3
Ol-5	13	8	mm_1–M_2
Ol-14	138	85	M_1–M_3
Sample 2–3			
Ol-2a	76	47	M_1–M_2
Ol-2b	166	102	M_1–M_2
Ol-3	50	31	mm_1–M_2
Ol-5	55	34	M_1–M_3
Ol-6	13	8	M_2–M_3
Sample 2–4			
Ol-23	35	21	M_1–M_3
Ol-20	73	45	M_1–M_3
Ol-19	23	14	M_1–M_2
Ol-18	52	32	M_1–M_2
Ol-17	10	6	M_1–M_3
Ol-14	35	21	M_1–M_3
Ol-9	16	10	M_1–M_3
Ol-8	23	14	mm_1–M_3
Ol-7	26	16	M_1–M_3
Ol-6b	105	65	M_1–M_2
Ol-6a	17	11	M_1–M_2
Ol-4	19	12	M_1–M_3
Ol-2	40	25	M_1–M_3
Ol-1	33	20	M_1–M_2
Sample 2–5			
Ol-3	13	8	M_1–M_3
Ol-12	102	63	M_1–M_3
Ol-11	75	46	M_0–M_2
Ol-7	26	16	mm_1–M_3
Ol-5	49	30	mm_1–M_3

dates of the SET1 (i.e. March 19, 1669) and SET2 (i.e. April 4, 1669) samples.

We observe that magma migration activity along the most prominent connection route M_1–M_5 (65 crystals; Fig. 7a), as recorded in the SET1 olivines, occurs over a range of timescales from 16 days to 1·5 years (Fig. 10b). The communication between the environments M_1 and M_5 started 1·5 years (October 1667) prior to eruption onset on March 11, 1669. Starting in October and becoming more frequent from November 1668, intrusion activity along this route rekindled and continued until shortly before the onset of eruptive activity (Fig. 11). Magma transfer along other, minor routes such as mm_1–M_5 (26 crystals; Fig. 7a), M_1–M_4 (14 crystals; Fig. 7a) and M_2–M_5 (seven crystals; Fig. 7a) occurred over shorter timescales (22 days to 8 months; Fig. 10b) starting between mid-October and early November 1668, and becoming more frequent towards the eruption onset (Fig. 11). We also find that the magma migration activity along M_1–M_5 decreased in the short term (i.e. days) before the onset of the eruption, as indicated by a decreasing number of crystals recording this event (Fig. 11).

The SET2 olivines record a different late-stage magmatic history, with the pathway M_1–M_3 (33 crystals; Fig. 7b) as the main transport route. Communication between the environments M_1 and M_3 commenced between mid- to late November 1668 and was soon followed by mixing activities along other, minor routes such as M_1–M_2 (17 crystals; Fig. 7b), mm_1–M_2 (8 crystals; Fig. 7b) and mm_1–M_3 (6 crystals; Fig. 7b). Timescales related to these minor connection routes are shorter (13 days to 3 months; Fig. 10b) and mixing occurred from mid-December 1668 (Fig. 11). Taking the number of crystals as evidence of intensity, we observe that the intrusive and mixing activity along all routes

increased in the short term (i.e. February 1669) both prior to and following the eruption onset (Fig. 11).

Occasionally, we also find rare olivine crystals ($n = 2$) that record entrainment of 'older' olivine cores of more mafic composition [i.e. M_0 ($= Fo_{79–82}$); see Kahl *et al.* (2015) for further details] from the surrounding crystal mush. These olivines are overgrown by more evolved rims of composition M_5 ($= Fo_{51–59}$) or M_2 ($= Fo_{70–72}$) and the corresponding timescales suggest that the crystals were entrained in their respective host melts sometime between late December 1668 and mid-January 1669. This coincides with the observed trend of increasing magma migration and/or mixing activity and the development of a branched shallow magma transport system commencing in November 1668 and continuing until the eruption onset (Fig. 11), with two dominant but diverging magma pathways (M_1–M_5 and M_1–M_3) as recorded by the SET1 and SET2–MtRs olivines.

PUTTING OBSERVATIONS INTO A MODEL: THE CHRONOLOGY OF MAGMATIC EVENTS

Combination of the information obtained from the systems analysis of the olivine zoning record and temporal information from modelling the diffusive relaxation of such zoning allows reconstruction of the sequence of magmatic events in the internal plumbing system of Etna volcano before and during the 1669 eruption. By considering the chemical stratigraphy preserved in 188 olivine crystals we can infer that olivine crystals resided in or interacted with six MEs prior to eruption (Fig. 7).

We observe that the vast majority (74%) of the olivine cores are connected to the dominant ME M_1 ($= Fo_{75–78}$) whose existence can be tracked throughout all studied eruption products (i.e. SET1, SET2–MtRs). The occurrence of large olivine cores with compositional plateaux predominantly at $Fo_{75–78}$ suggests that the crystals have resided in M_1 for a significant period of time before moving on to other MEs. Furthermore, we find that these core compositional plateaux form groups or clusters in variation diagrams (Fig. 5e and g). Taking the extent of the observed compositional plateaux as evidence, we infer that the instantaneous ambient conditions within M_1 were held constant during the crystallization of olivine cores. Such constant conditions can exist, for example, within a large reservoir (e.g. sill or dyke) without large-scale convection. We suggest that a reservoir M_1 existed at shallow levels ($P \leq 1$ kbar) within Etna's plumbing system, containing a partially degassed melt (up to 1·1 wt %; ~5·1 wt % MgO) in equilibrium with olivine ($Fo_{75–78}$), clinopyroxene (Mg# 81–83), plagioclase ($An_{66–75}$) and Fe–Ti oxide ($Mt_{35–52}$ depending on the fO_2: QFM or NNO buffer) at temperatures $\leq$1170°C. The depth range ($\leq$1 kbar; $\leq$3 km) at which M_1 olivine cores can be formed correlates with the top part of a main magma storage volume (Fig. 12a) that was identified between ~2 m below sea level (b.s.l.) and 8–9 km (b.s.l.) (e.g. Bonaccorso *et al.*, 2011; Patanè *et al.*, 2013). This body lies along the western border of the high-V_p body (HVB) (Aloisi *et al.*, 2002; Patanè *et al.*, 2003, 2006) and is interpreted as the

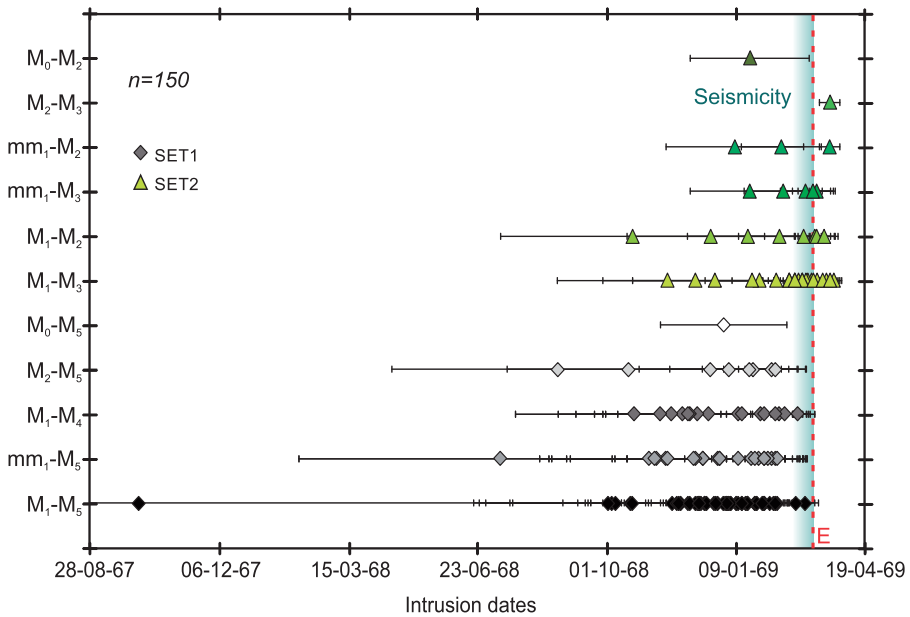

Fig. 11. Calculated timescales of intrusive events into Etna's shallow plumbing system along different transport routes. Coloured symbols refer to intrusion times along different transport pathways calculated by subtracting the mixing timescales from the eruption dates of SET1 (i.e. March 19, 1669) and SET2 (i.e. April 4, 1669) samples. Black symbols refer to intrusion times related to rarely connected MEs such as M_0–M_5, M_0–M_2 and M_2–M_3 [M_0 ($= Fo_{79–83}$), not displayed in Fig. 7]. Red dashed line (E) marks the overall eruption onset (i.e. March 11, 1669); shaded area indicates the approximate range of seismic activity preceding the onset of the 1669 eruption. Contemporary records reported that vigorous seismicity preceded the eruption by *c.* 2 weeks and that earthquake intensity increased in the days (starting on March 8, 1669) prior to the eruption onset (e.g. Mulas *et al.*, 2016, and references therein).

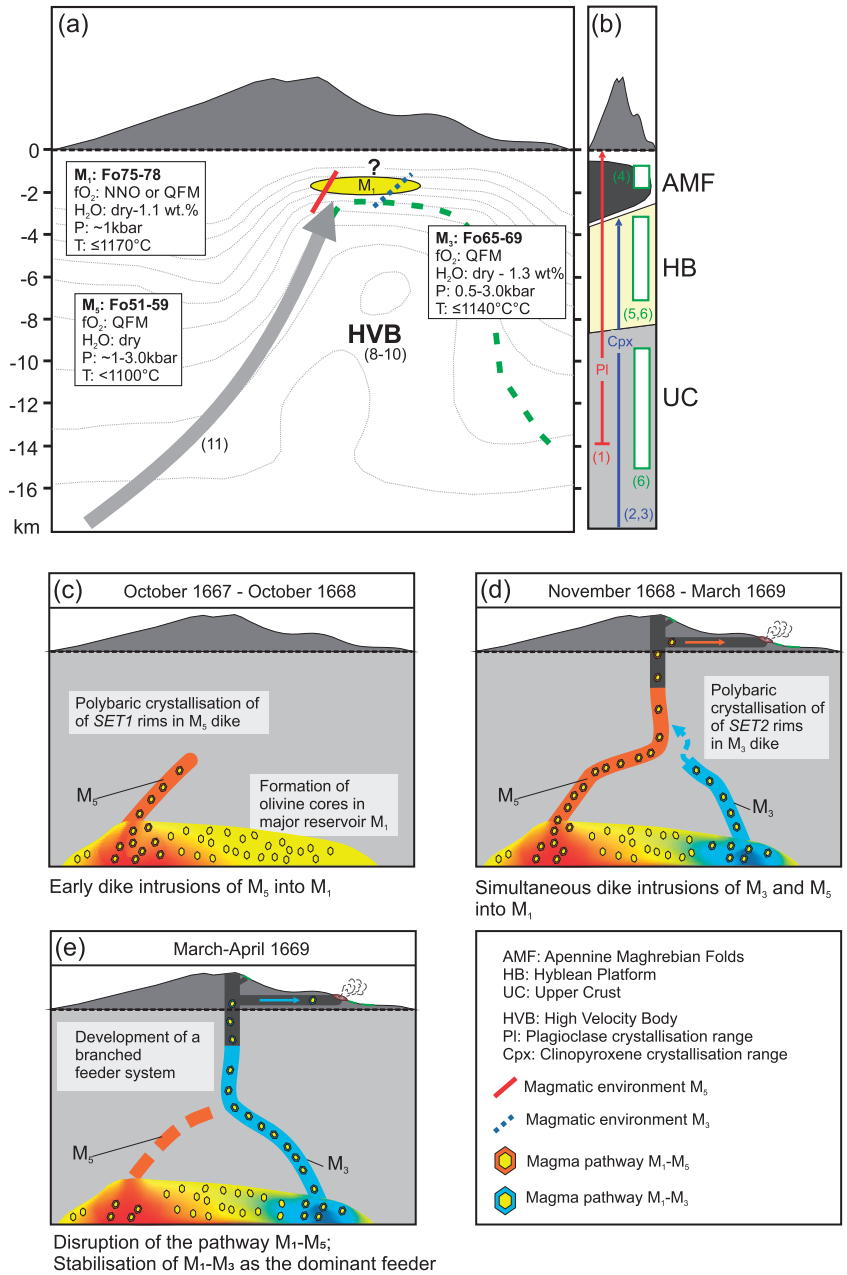

Fig. 12. (a) Schematic illustration depicting the approximate depth of the reservoir M_1 and the dyke-like environments M_5 and M_3 in which the SET1 (M_5) and the SET2–MtRs (M_3) olivine rims formed. Insets list the physical conditions of the three environments obtained by thermodynamic modelling using rhyolite-MELTS. For comparison, the depths contours of the high-V_p body [HVB; (8) Aloisi *et al.*, 2002; (9, 10) Patanè *et al.*, 2003, 2006] and the consensus main magma pathway (grey arrow) [(11) Patanè *et al.*, 2013] are shown. (b) Schematic reconstruction of Etna's vertical feeding system (from Giacomoni *et al.*, 2014, 2016) based on plagioclase and clinopyroxene crystallization depths [(1) Giacomoni *et al.*, 2014; (2) Giacomoni *et al.*, 2016; (3) Armienti *et al.*, 2013]. Vertical bars represent the depth range of low-velocity zones detected by (4) Bonaccorso *et al.* (2011), (5) Lundgren *et al.* (2003) and (6) Murru *et al.* (1999). For comparison the major stratigraphic units (AMF, Apennine Maghrebian folds; HB, Hyblean Platform; UC, upper crust) underlying Mt Etna are shown. (c–e) Schematic reconstruction of the sequence and chronology of magmatic events in the internal plumbing of Mt Etna before and during the 1669 flank eruption. (c) Dyke intrusions of M_5-type magma into the major reservoir M_1 (= $Fo_{75–78}$) commenced 1·5 years prior to the eruption onset. From October 1668 repeated dyke injections of M_5 into M_1 resulted in the formation of the SET1 olivine rims. (d) Starting in November 1668, a new batch of magma (M_3-type) intruded the reservoir M_1 as recorded in the chemical stratigraphy of the SET2 olivines. Intrusions of M_3-type magma into M_1 resulted in the formation of the SET2 olivine rims. In the months and weeks prior to the eruption, simultaneous injections of M_5- and M_3-type magma into the M_1 reservoir occurred, and they continued until the eruption onset. A branched feeder system with two dominant but diverging magma transport routes M_1–M_5 and M_1–M_3 developed. (e) Change of magma transport dynamics shortly after the beginning of the 1669 flank eruption resulted in the disruption of the pathway M_1–M_5 and the stabilization of the transport route M_1–M_3, which facilitated syn-eruptive magma recharge and magma mixing in the weeks following the eruption onset. (See main text for further details.)

consensus main pathway for magma transport and magma accumulation at Mt Etna (e.g. Patanè *et al.*, 2013).

The 1669 (SET1 and SET2–MtRs) olivine rims are more diverse in composition, ranging from Fo_{51} to Fo_{78}, and form distinct trends in variation diagrams (Fig. 5d and f) indicating that the conditions under which the olivine rims formed were more variable. Our MELTS modelling results suggest that the SET1 ($M_5 = Fo_{51–59}$) and SET2 ($M_3 = Fo_{65–69}$) rim populations can be obtained over a much broader pressure range (0·5–3·0 kbar) and variable water conditions (dry to 1·3 wt %). Taking these observations as evidence, we think that the SET1 and SET2–MtRs olivine rims could reflect crystallization under polybaric conditions within two different environments M_5 and M_3, which are characterized by variable temperatures, water contents and oxygen fugacity conditions. Polybaric crystallization of SET1 and SET2–MtRs olivine rims agrees with findings from textural, compositional and thermobarometric studies of Etna plagioclase and clinopyroxene (Armienti *et al.*, 2013; Giacomoni *et al.*, 2014, 2016). These studies suggest that clinopyroxene and plagioclase crystallization—although starting at different depths (Fig. 12b)—occurs continuously under polybaric conditions through a vertically extended feeding system containing different magma crystallization levels (Armienti *et al.*, 2013; Giacomoni *et al.*, 2014, 2016). The stability field of plagioclase and clinopyroxene further indicates a large variability of the water content within Etna's plumbing system (Giacomoni *et al.*, 2014, 2016). This observation agrees with the variable water contents under which the different olivine rim and core populations identified in this and previous studies (Kahl *et al.*, 2015) could be obtained via thermodynamic modelling.

Combining the above observations with the temporal record obtained from diffusion modelling of 150 olivine crystals, we can derive the following schematic scenario of magmatic events in the plumbing system of Mt Etna that could have led to the 1669 flank eruption.

We propose that after the formation of the olivine cores under relatively constant conditions, possibly within a larger reservoir M_1 located at relatively shallow levels ($P \leq 1$ kbar; ≤ 3 km) within Etna's plumbing system, the reservoir was intruded by a batch of more evolved, degassed and possibly aphyric M_5-type magma (Fig. 12c). From the comprehensive timescale record ($n = 109$) of the SET1 olivines, we observe that intrusions into M_1 occurred as early as 1·5 years (October 1667) prior to the eruption onset. From October 1668, these injections became more frequent, and the SET1 olivine rims began crystallizing. Owing to the fact that M_5 olivines form only rims, and never occur as cores in the SET1 samples, plus considering the broad pressure range under which they can be formed, we suggest that the M_5 environment could represent a feeder dyke or conduit. SET1 olivine rims grew in this conduit as it transected the M_1 reservoir and propagated further to the surface (Fig. 12c). This scenario would agree with the lack of M_5-type olivine cores and would also explain why the rims can be obtained over a broader pressure interval.

The steady replenishment of M_1 that began in October 1668 and continued until shortly before the eruption onset probably fluidized and eroded the surrounding magma mush, resulting in the formation of a local 'mixing bowl' (Bergantz *et al.*, 2015; Schleicher *et al.*, 2016) within the reservoir M_1. The formation of such a mixing bowl is evidenced by the core and rim compositions of a minor subset of olivines from the SET1 samples, which refer to the MEs M_4 ($= Fo_{60–65}$), M_2 ($= Fo_{70–72}$) and mm_1 ($= Fo_{73–75}$). The existence of such a local mixing bowl is further underpinned by the corresponding timescale determinations (Fig. 11). We observe, for example, that a major intrusive event (i.e. M_1–M_5) is followed by a delay of only a few days or weeks by a mixing (e.g. M_1–M_4) or entrainment (e.g. M_2–M_5 and mm_1–M_5) event involving a subset of crystal cores or rims that formed in these minor magmatic environments (Fig. 11). In this sense, we think that these minor ME connections identified in systems analysis of the SET1 olivines (Fig. 7a), refer to local mixing trajectories reflecting fluidization and/or mixing within the M_1 reservoir as time proceeds. Starting in November 1668, only a few weeks after the first intrusive episode into the M_1 reservoir, a second pulse of magma injections (M_3-type magma) is observed. However, this time the intrusive event is recorded by the SET2 olivines, and marks the onset of simultaneous magma injections, along two different pathways (M_1–M_5 and M_1–M_3), into the mutual reservoir M_1 (Fig. 12d). The intrusion frequency of M_3-type magma into M_1 increased notably from December 1668, and is again followed by mixing activities along minor connection routes (Fig. 11). As mentioned above, the steady injections of M_3 probably caused the formation of another, localized 'mixing bowl' within M_1, in which the surrounding magma mush was fluidized and eroded. This again is evidenced by a minor subset of core and rim populations recognized in the SET2 (and MtRs) olivines [i.e. mm_1 ($= Fo_{73–75}$), M_2 ($= Fo_{70–72}$)] and a short delay in the corresponding timescale record (Fig. 11). Similar to the M_5-type olivine rims observed in the SET1 samples, we find that the M_3-type rims can form under variable conditions (i.e. temperature $\leq 1140°C$, dry to 1·3 wt % water contents, pressure 0·5–3·0 kbar). We assume therefore that the environment M_3 could represent a second feeder dyke in which the M_3-type olivine rims started to crystallize [possibly together with clinopyroxene (Mg# 74–79), plagioclase ($An_{53–64}$) and Fe–Ti oxides ($Mt_{43–52}$)] when the dyke intersected the major reservoir M_1, where the previously formed olivine cores were picked up (Fig. 12d).

The simultaneous recharge of the reservoir M_1, along the two different routes M_1–M_5 and M_1–M_3, increased steadily from November 1668 (evidenced by the large number of crystals tracking these events) and

remained high in the weeks and days prior to the eruption onset on March 11, 1669 (Fig. 11). We observe, however, that in the days immediately before the eruption, the number of crystals recording the recharge of M_5 into M_1 decreased (Fig. 11). We speculate that the steady replenishment of M_1, in the months and weeks prior to the eruption, could have enhanced the build-up of overpressure inside the reservoir. This may have resulted in the opening of a new fracture system that gave rise to the development of a branched shallow feeder system with two dominant, but diverging, magma pathways (M_1–M_5 and M_1–M_3) facilitating the sequential transfer of magma into the main conduit system (Fig. 12d and e). We note that seismicity increased *c.* 2 weeks (e.g. Tanguy & Patanè, 1996; Mulas *et al.*, 2016, and references therein) before the eruption onset, and we suggest that this could be related to SET1 magma intruding the main conduit system. Then, in the early hours of March 11, a dry fracture system opened on the south flank of Etna, between Mt Frumento (2800 m a.s.l.) and Piano San Leo (1200 m a.s.l.), allowing lateral draining of the SET1 magma and starting the eruption (Mulas *et al.*, 2016, and references therein) (Fig. 12e).

Following the eruption of the SET1 samples, the injection frequency of M_3 into M_1 remained high and persisted throughout the eruption onset as recorded by the SET2 olivines (Fig. 11). It appears that shortly after the eruption onset, the local magma transfer dynamics changed, resulting in the disruption of the dominant pathway M_1–M_5, as indicated by a decreasing number of SET1 olivines tracking this history. Instead, the pathway M_1–M_3 became a dominant feeder that promoted syn-eruptive recharge and mixing in the weeks following the eruption onset (Fig. 12e), resulting in the eruption of the SET2 (and MtRs) magma.

We can only speculate about the causes for the change in transfer dynamics. One possible explanation could be a pressure-induced change of the local stress field caused by the system inflating with magma and repeated dyke injections (e.g. Bonafede & Danesi, 1997; Acocella & Neri, 2003) of M_3 into M_1. Alternatively, it could be that the supply of M_5 magma simply decreased, resulting in the interruption of the M_1–M_5 pathway.

We want to stress here that although the development of a branched feeder system is only one possible scenario that can account for the events recorded in the chemical stratigraphy of the 1669 olivines, it is not without precedent. Kahl *et al.* (2013) observed for the 2006 summit eruptions that differences in the connectivity patterns of zoned olivine populations existed for the July and October episodes. They proposed that these could have been due to fluctuations in the prevalent magma transport regime. They concluded that such short-term fluctuations—occurring within months of each other—could be associated with modifications of the shallow plumbing system; this would be an analogous event to that proposed for 1669. As further evidence, the olivine rims of SET1 and SET2 track divergent late-stage magmatic histories (M_1–M_5 and M_1–M_3) that are inconsistent with the progressive emptying of a mixed or hybrid reservoir.

CONCLUSIONS

We have applied a three-way integrated method linking a systems analysis with a time-integrated study of zoned olivine populations and a forward modelling approach using thermodynamic calculations with rhyolite-MELTS to constrain the nature and dynamics of magma transfer and magma mixing before and during the 1669 flank eruption of Etna volcano. Systems analysis of the compositional zoning record preserved in 202 olivine crystals revealed the existence of three distinct Magmatic Environments (MEs) in which the majority of the olivine cores [M_1 ($=Fo_{75–78}$)] and rims [i.e. M_5 ($=Fo_{51–59}$) and M_3 ($=Fo_{65–69}$)] formed. Application of thermodynamic calculations with the rhyolite-MELTS software allowed constraint of the key intensive variables associated with these MEs. We found that temperature, water content and oxidation state are the main distinguishing features of the different MEs.

Olivine cores ($\sim Fo_{75–78}$) formed in a partially degassed environment M_1 together with clinopyroxene (Mg# 81–83), plagioclase ($An_{66–75}$) and, depending on the fO_2 (QFM or NNO), Fe–Ti oxides ($Mt_{35–52}$), at temperatures $\leq$1170°C and pressures $<$1 kbar. The different rim populations identified in the SET1 and SET2–MtRs olivines indicate diverging magmatic histories following the core formation, suggesting a bifurcated magma feeder system for the 1669 eruption. We find that SET1 rims (i.e. $Fo_{51–59}$) can form under dehydrated and QFM oxygen fugacity conditions at temperatures $<$1100°C, in equilibrium with evolved clinopyroxenes (Mg# 72–74). The less evolved SET2 olivine rims ($=Fo_{65–69}$) can be obtained at QFM or NNO oxygen fugacity conditions, at temperatures $\leq$1140°C, under variable water contents (dry to 1·3 wt %), together with clinopyroxene (Mg# 74–79), plagioclase ($An_{53–64}$) and Fe–Ti oxides ($Mt_{43–52}$).

Importantly, olivine cores define compositional plateaux formed under relatively uniform conditions, whereas olivine rims define broad compositional ranges that can form over a broad pressure range (0·5–3·0 kbar). This suggests that olivine cores formed under relatively constant conditions, possibly within a larger reservoir M_1 that was located at shallow levels ($\leq$1 kbar) within Etna's plumbing system, and olivine rims formed in dykes (M_3 and M_5) transecting the large M_1 reservoir. These results reinforce the idea of a multi-level, vertically zoned feeding system at Mount Etna, where magma can continuously experience variable chemical–physical conditions.

Application of diffusion modelling to the zoned olivine crystals allowed us to reconstruct the timing and chronology of melt and crystal transfer prior to and during the 1669 flank eruption. We find that the pathway M_1–M_5 was established 1·5 years prior to eruptive

activity. In addition, the parallel M_1–M_5 recharge increased notably in the months prior to eruption onset. For several weeks a bifurcated transport system with two dominant magma pathways developed along M_1–M_5 and M_1–M_3 dyke injections. Accompanied by vigorous seismicity, in the days immediately prior to eruption the local magma transfer dynamics changed and the M_1–M_5 recharge activity slowed down. M_1–M_3 recharge remained high and persisted throughout the eruption onset on March 11, which drained SET1 lavas. In the weeks following the eruption onset, the pathway M_1–M_3 became the dominant feeder dyke, promoting syn-eruptive recharge and mixing in the shallow plumbing system culminating in the eruption of the later SET2 lavas.

In conclusion, the three-way integrated approach used in this study allows the reconstruction of the evolutionary history of a temporally remote and hazardous flank eruption not accessible by means of conventional volcano monitoring techniques. Combination of pre-existing and state-of-the-art petrological tools allowed us to track the magmatic events that led to the 1669 eruption and to decipher changes in the local magma transfer dynamics that immediately preceded the eruption onset. Forward thermodynamic modelling linked with a time-integrated study allowed us to recover pre- and syn-eruptive magma storage conditions and timescales within different magma reservoirs located in the shallow plumbing system of Mt Etna. Most importantly, we demonstrate that the time elapsed between magma injections into the shallow plumbing system and accumulation and remobilization of eruptible magma is of the order of months to weeks only.

SUPPLEMENTARY DATA

Supplementary data for this paper are available at *Journal of Petrology* online.

ACKNOWLEDGEMENTS

This paper has benefited greatly from comments by G. Bergantz, N. Métrich and an anonymous reviewer. We thank A. Lumsden and M. Wilson for the editorial handling of the paper and for helpful comments. We are grateful to D. Müller (LMU Munich), D. Aßbichler (LMU Munich), R. Walshaw and G. Lloyd (University of Leeds) for assistance with EMP, XRF and EBSD analysis. We wish to thank S. Chakraborty for useful suggestions and discussions on the paper.

FUNDING

This work was supported by an ERC Advanced Grant EVOKES (247076) to D.B.D. M.K. acknowledges two postdoctoral research fellowship grants of the Deutsche Forschungsgemeinschaft (DFG) (KA 3532/1-1) and the Icelandic Centre for Research (Rannís) (152726-051). T.U. acknowledges funding from Science Foundation Ireland grant SFI/12/ERC/E2499.

REFERENCES

Acocella, V. & Neri, M. (2003). What makes flank eruptions? The 2001 Etna eruption and its possible triggering mechanisms. *Bulletin of Volcanology* **65**, 517–529.

Albert, H., Costa, F. & Marti, J. (2015). Timing of magmatic processes and unrest associated with mafic historical monogenetic eruptions in Tenerife Island. *Journal of Petrology* **56**, 1945–1966.

Allard, P., Behncke, B., D'Amico, S., Neri, S. & Gambino, S. (2006). Mount Etna 1993–2005: Anatomy of an evolving eruptive cycle. *Earth-Science Reviews* **78**, 85–114.

Aloisi, M., Cocina, O., Neri, G., Orecchio, B. & Privitera, E. (2002). Seismic tomography of the crust underneath the Etna volcano, Sicily. *Physics of the Earth and Planetary Interiors* **134**, 139–155.

Andronico, D., Branca, S., Calvari, S., Burton, M., Caltabiano, T., Corsaro, R. A., Del Carlo, P., Garfì, G., Lodato, L., Miraglia, L., Murè, F., Neri, M., Pecora, E., Pompilio, M., Salerno, G. & Spampinato, L. (2005). A multi-disciplinary study of the 2002–03 Etna eruption: insights into a complex plumbing system. *Bulletin of Volcanology* **67**, 314–330.

Armienti, P., Innocenti, F., Petrini, R., Pompilio, M. & Villari, L. (1988). Sub-aphyric alkali basalt from Mt. Etna: inferences on the depth and composition of the source magma. *Rendiconti della Società Italiana de Mineralogia e Petrologia* **43**, 877–891.

Armienti, P., Perinelli, C. & Putirka, K. D. (2013). A new model to estimate deep-level magma ascent rates with application to Mt. Etna (Sicily, Italy). *Journal of Petrology* **54**, 795–813.

Asimow, P. D. & Ghiorso, M. S. (1998). Algorithmic modifications extending MELTS to calculate sub-solidus phase relations. *American Mineralogist* **83**, 1127–1131.

Barbieri, M., Cristofolini, R., Delitala, M. C., Fornaseri, M., Romano, R., Taddeucci, A. & Tolomeo, L. (1993). Geochemical and Sr-isotope data on historical lavas of Mount Etna. *Journal of Volcanology and Geothermal Research* **56**, 57–69.

Behncke, B. & Neri, M. (2003). The July–August 2001 eruption of Mt. Etna (Sicily). *Bulletin of Volcanology* **65**, 461–476.

Bergantz, G. W., Schleicher, J. M. & Burgisser, A. (2015). Open-system dynamics and mixing in magma mushes. *Nature Geoscience* **8**, 793–796.

Bonaccorso, A., Bonforte, A., Currenti, G., Del Negro, C., Di Stefano, A. & Greco, F. (2011). Magma storage, eruptive activity and flank instability: Inferences from ground deformation and gravity changes during the 1993–2000 recharging of Mt. Etna volcano. *Journal of Volcanology and Geothermal Research* **200**, 245–254.

Bonafede, M. & Danesi, S. (1997). Near-field modifications of stress induced by dyke injection at shallow depth. *Geophysical Journal International* **130**, 435–448.

Borelli, G. A. (1670). *Historia et meteorologia incendii aetnaei anni 1669*. Officina Dominici Ferri, 162 pp.

Branca, S. & Del Carlo, P. (2004). Eruptions of Mt. Etna during the past 3200 years: A revised compilation integrating the historical and stratigraphic records. In: Bonaccorso, A., Calvari, S., Coltelli, M., Del Negro, C. & Falsaperla, S. (eds) *Mt. Etna: Volcano Laboratory. American Geophysical Union, Geophysical Monograph* **143**, 1–27.

Branca, S., Coltelli, M. & Groppelli, G. (2011). Geological evolution of a complex basaltic stratovolcano: Mt. Etna, Italy. *Italian Journal of Geosciences* **130**, 306–317.

Branca, S., De Beni, E. & Proietti, C. (2013). The large and destructive 1669 AD eruption at Etna volcano: reconstruction of the lava flow field evolution and effusion rate trend. *Bulletin of Volcanology* **75**, 694.

Branca, S. Azzaro, R., De Beni, E., Chester, D. & Duncan, A. (2015). Impacts of the 1669 eruption and the 1693 earthquakes on the Etna Region (Eastern Sicily, Italy): An example of recovery and response of a small area to extreme events. *Journal of Volcanology and Geothermal Research* **303**, 25–40.

Calvari, S., Coltelli, M., Neri, M., Pompilio, M. & Scribano, V. (1994). The 1991–1993 Etna eruption: chronology and lava flow-field evolution. *Acta Vulcanologica* **4**, 1–14.

Carrera, P. (1636). *Il Mongibello descritto in tre libri*. nel Palazzo dell'Illustrissimo Senato, per Gio. Rossi, 204 pp.

Chester, D. K., Duncan, A. M., Guest, J. E. & Kilburn, C. R. J. (1985). *Mount Etna. The Anatomy of a Volcano*. Chapman & Hall.

Chew, D. M., Babechuk, M. G., Cogné, N., Mark, C., O'Sullivan, G., Henrichs, I., Doepke, D. & McKenna, C. A. (2016). (LA,Q)-ICPMS trace-element analyses of Durango and McClure Mountain apatite and implications for making natural LA-ICPMS mineral standards. *Chemical Geology* **435**, 35–48.

Clark, A. M. & Long, J. V. P. (1971). The anisotropic diffusion of nickel in olivine. In: Sherwood, J. N., Chadwick, A. V., Muir, W. M. & Swinton, F. L. (eds) *Diffusion Processes*. Gordon & Breach, pp. 511–521.

Clocchiatti, R. & Métrich, N. (1984). La cristallisation des pyroclastes des éruptions étnéennes de 1669 (Mt Rossi) et 1892 (Mt Silvestri). Témoignages de contamination. *Bulletin of Volcanology* **47**, 908–928.

Clocchiatti, R., Joron, J. L. & Treuil, M. (1988). The role of selective alkali contamination in the evolution of recent historic lavas of Mt. Etna. *Journal of Volcanology and Geothermal Research* **34**, 241–249.

Condomines, M., Tanguy, J. C. & Michaud, V. (1995). Magma dynamics at Mount Etna: constraints from U–Th–Ra–Pb radioactive disequilibria and Sr isotopes in historical lavas. *Earth and Planetary Science Letters* **132**, 297–314.

Corsaro, R. A., Cristofolini, R. & Patanè, L. (1996). The 1669 eruption at Mount Etna: chronology, petrology and geochemistry, with inferences on the magma sources and ascent mechanisms. *Bulletin of Volcanology* **58**, 348–358.

Corsaro, R. A., Miraglia, L. & Pompilio, M. (2007). Petrologic evidence of a complex plumbing system feeding the July–August 2001 eruption of Mt. Etna, Sicily, Italy. *Bulletin of Volcanology* **69**, 401–421.

Corsaro, R. A., Métrich, N., Allard, P., Andronico, D., Miraglia, L. & Fourmentraux, C. (2009). The 1974 flank eruption of Mount Etna: An archetype for deep dike-fed eruptions at basaltic volcanoes and a milestone in Etna's recent history. *Journal of Geophysical Research* **114**, B07204.

Costa, F. & Chakraborty, S. (2004). Decadal time gaps between mafic intrusion and silicic eruption obtained from chemical zoning patterns in olivine. *Earth and Planetary Science Letters* **227**, 517–530.

Costa, F., Dohmen, R. & Chakraborty, S. (2008). Timescales of magmatic processes from modelling the zoning patterns of crystals. In: Putirka, K. D. & Tepley, F. J., III (eds) *Minerals, Inclusions and Volcanic Processes. Mineralogical Society of America and Geochemical Society, Reviews in Mineralogy and Geochemistry* **69**, 545–594.

Deer, W. A., Howie, R. A. & Zussman, J. (2013). *An Introduction to the Rock-Forming Minerals*. London: Mineralogical Society of Great Britain and Ireland, 510 pp.

Doglioni, C., Innocenti, F. & Mariotti, G. (2001). Why Mt. Etna? *Terra Nova* **13**, 25–31.

Dohmen, R. & Chakraborty, S. (2007). Fe–Mg diffusion in olivine II: point defect chemistry, change of diffusion mechanisms and a model for calculation of diffusion coefficients in natural olivine. *Physics and Chemistry of Minerals* **34**, 409–430.

Dohmen, R., Becker, H.-W. & Chakraborty, S. (2007). Fe–Mg diffusion in olivine I: experimental determination between 700 and 1,200°C as a function of composition, crystal orientation and oxygen fugacity. *Physics and Chemistry of Melts* **34**, 389–407.

Ferlito, C., Viccaro, M., Nicotra, E. & Cristofolini, R. (2012). Regimes of magma recharge and their control on the eruptive behaviour during the 2001–2005 period at Mt. Etna (Italy). *Bulletin of Volcanology* **74**, 533–543.

Ferrara, F. (1818). *Descrizione dell'Etna con la storia delle eruzioni e il catalogo dei prodotti*. Presso Lorenzo Dato, 256 pp.

Giacomoni, P. P., Ferlito, C., Coltorti, M., Bonadiman, C. & Lanzafame, G. (2014). Plagioclase as archive of magma ascent dynamics on 'open conduit' volcanoes: The 2001–2006 eruptive period at Mt. Etna. *Earth-Science Reviews* **138**, 371–393.

Giacomoni, P. P., Coltorti, M., Bryce, J. G., Fahnestock, M. F. & Guitreau, M. (2016). Mt. Etna plumbing system revealed by combined textural, compositional, and thermobarometric studies in clinopyroxenes. *Contributions to Mineralogy and Petrology* **171**, 34.

Ghiorso, M. S. & Gualda, G. A. R. (2015). An H_2O–CO_2 mixed fluid solubility model compatible with rhyolite-MELTS. *Contributions to Mineralogy and Petrology* **169**, 53.

Ghiorso, M. S. & Sack, R. O. (1995). Chemical mass transfer in magmatic processes. IV. A revised and internally consistent thermodynamic model for the interpolation and extrapolation of liquid–solid equilibria in magmatic systems at elevated temperatures and pressures. *Contributions to Mineralogy and Petrology* **119**, 197–212.

Gillot, P. Y., Kieffer, G. & Romano, R. (1994). The evolution of Mount Etna in the light of potassium–argon dating. *Acta Vulcanologica* **5**, 81–87.

Gualda, G. A. R., Ghiorso, M. S., Lemons, R. V. & Carley, T. L. (2012). Rhyolite-MELTS: A modified calibration of MELTS optimized for silica-rich, fluid-bearing magmatic systems. *Journal of Petrology* **53**, 875–890.

Guest, J. E. & Duncan, A. M. (1981). Internal plumbing of Mount Etna. *Nature* **290**, 584–586.

Gvirtzman, Z. & Nur, A. (1999). The formation of Mount Etna as the consequence of slab rollback. *Nature* **401**, 782–785.

Hartley, M. E., Morgan, D. J., Maclennan, J., Edmonds, M. & Thordarson, T. (2016). Tracking timescales of short-term precursors to large basaltic fissure eruptions through Fe–Mg diffusion in olivine. *Earth and Planetary Science Letters* **439**, 58–70.

Hughes, J. W., Guest, J. E. & Duncan, A. M. (1990). Changing styles of effusive eruption on Mount Etna since AD 1600. In: Ryan, M. P. (ed.) *Magma Transport and Storage*. Wiley, pp. 385–405.

Jochum, K. P., Weis, U., Stoll, B., Kuzmin, D., Yang, Q., Raczek, I., Jacob, D. E., Stracke, A., Birbaum, K., Frick, D. A., Günther, D. & Enzweiler, J. (2011). Determination of reference values for NIST SRM 610–617 glasses following ISO guidelines. *Geostandards and Geoanalytical Research* **35**, 397–429.

Kahl, M., Chakraborty, S., Costa, F. & Pompilio, M. (2011). Dynamic plumbing system beneath volcanoes revealed by kinetic modelling and the connection to monitoring data: an example from Mt. Etna. *Earth and Planetary Science Letters* **308**, 11–22.

Kahl, M., Chakraborty, S., Costa, F., Pompilio, M., Liuzzo, M. & Viccaro, M. (2013). Compositionally zoned crystals and real-

time degassing data reveal changes in magma transfer dynamics during the 2006 summit eruptive episodes of Mt. Etna. *Bulletin of Volcanology* **75**, 692.

Kahl, M., Chakraborty, S., Pompilio, M. & Costa, F. (2015). Constraints on the nature and evolution of the magma plumbing system of Mt. Etna Volcano (1991–2008) from a combined thermodynamic and kinetic modelling of the compositional record of minerals. *Journal of Petrology* **56**, 2025–2068.

Landi, P., Francalanci, L., Pompilio, M., Rosi, M., Corsaro, R. A., Petrone, C. M., Nardini, I. & Miraglia, L. (2006). The December 2002–July 2003 effusive event at Stromboli volcano, Italy: an insight into the shallow plumbing system by petrochemical studies. *Journal of Volcanology and Geothermal Research* **155**, 263–284.

Lanzafame, G., Neri, M., Acocella, V., Billi, A., Funiciello, R. & Giordano, G. (2003). Structural features of the July–August 2001 Mount Etna eruption: evidence for a complex magma supply system. *Journal of the Geological Society, London* **160**, 531–544.

Larrea, P., França, Z., Lago, M., Widom, E., Galé, C. & Ubide, T. (2013). Magmatic processes and the role of antecrysts in the genesis of Corvo Island (Azores Archipelago, Portugal). *Journal of Petrology* **54**, 769–793.

Loucks, R. R. (1996). A precise olivine–augite Mg–Fe-exchange geothermometer. *Contributions to Mineralogy and Petrology* **125**, 140–150.

Lundgren, P., Berardino, P., Coltelli, M., Fornaro, G., Lanari, R., Puglisi, G., Sansosti, E. & Tesauro, M. (2003). Coupled magma chamber inflation and sector collapse slip observed with synthetic aperture radar interferometry on Mt. Etna volcano. *Journal of Geophysical Research* **108**, 2247–2267.

Mancino, C. (1669). *Narrativa del fuoco uscito da Mongibello il dı undici di marzo del 1669*. Giuseppe Bisagni.

Métrich, N. & Clocchiatti, R. (1989). Melt inclusion investigation of the volatile behaviour in historic alkali basaltic magmas of Etna. *Bulletin of Volcanology* **51**, 185–198.

Métrich, N. & Clocchiatti, R. (1996). Sulphur abundance and its speciation in oxidized alkaline melts. *Geochimica et Cosmochimica Acta* **60**, 4151–4160.

Métrich, N. & Rutherford, M. J. (1998). Low pressure crystallization paths of H_2O-saturated basaltic–hawaiitic melts from Mt Etna: Implications for open-system degassing of basaltic volcanoes. *Geochimica et Cosmochimica Acta* **62**, 1195–1205.

Métrich, N., Allard, P., Spilliaert, N., Andronico, D. & Burton, M. (2004). 2001 flank eruption of the alkali and volatile-rich primitive basalt responsible for Mount Etna's evolution in the last three decades. *Earth and Planetary Science Letters* **228**, 1–17.

Mulas, M., Cioni, R., Andronico, D. & Mundula, F. (2016). The explosive activity of the 1669 Monti Rossi eruption at Mt. Etna (Italy). *Journal of Volcanology and Geothermal Research* **328**, 115–133.

Murru, M., Montuori, C., Wyss, M. & Privitera, E. (1999). The locations of magma chambers at Mt. Etna, Italy, mapped by b-values. *Geophysical Research Letters* **26**, 2553–2556.

Nicotra, E. & Viccaro, M. (2012). Unusual magma storage conditions at Mt. Etna (Southern Italy) as evidenced by plagioclase megacryst-bearing lavas: implications for the plumbing system geometry and summit caldera collapse. *Bulletin of Volcanology* **74**, 795–815.

Patanè, D., De Gori, P., Chiarabba, C. & Bonaccorso, A. (2003). Magma ascent and the pressurisation of Mt. Etna's volcanic system. *Science* **299**, 2061–2063.

Patanè, D., Barberi, G., Cocina, O., De Gori, P. & Chiarabba, C. (2006). Time resolved seismic tomography detects magma intrusions at Mount Etna. *Science* **313**, 821–825.

Patanè, D., Aiuppa, A., Aloisi, M., Behncke, B., Cannata, A., Coltelli, M., Di Grazia, G., Gambino, S., Gurrieri, S., Mattia, M. & Salerno, G. (2013). Insights into magma and fluid transfer at Mount Etna by a multiparametric approach: A model of the events leading to the 2011 eruptive cycle. *Journal of Geophysical Research: Solid Earth* **118**, 3519–3539.

Paton, C., Hellstrom, J., Paul, B., Woodhead, J. & Hergt, J. (2011). Iolite: freeware for the visualization and processing of mass spectrometric data. *Journal of Analytical Atomic Spectrometry* **26**, 2508–2518.

Pompilio, M. & Rutherford, M. J. (2002). Pre-eruption conditions and magma dynamics of recent amphibole-bearing Etna basalt. American Geophysical Union, Fall Meeting 2002, Abstracts V61A-1354.

Prior, D. J., Boyle, A. P., Brenker, F., Cheadle, M. C., Day, A., Lopez, G., Peruzzo, L., Potts, G. J., Reddy, S., Spiess, R., Timms, N. E., Trimby, P., Wheeler, J. & Zetterstrom, L. (1999). The application of electron backscatter diffraction and orientation contrast imaging in the SEM to textural problems in rocks. *American Mineralogist* **84**, 1741–1759.

Rae, A. S. P., Edmonds, M., Maclennan, J., Morgan, D., Houghton, B., Hartley, M. E. & Sides, I. (2016). Time scales of magma transport and mixing at Kilauea Volcano, Hawai'i. *Geology* **44**, 463–466.

Recupero, G. (1815). *Storia naturale e generale dell'Etna*. Stamperia della Regia Università degli Studi, doi:10.3931/e-rara-11880.

Rittmann, A. (1965). Notizie sull'Etna. *Nuovo Cimento Supplement* **3**, 1117–1123.

Sakyi, P. A., Tanaka, R., Kobayashi, K. & Nakamura, E. (2012). Inherited Pb isotopic records in olivine antecryst-hosted melt inclusions from Hawaiian lavas. *Geochimica et Cosmochimica Acta* **95**, 169–195.

Schiano, P., Clocchiatti, R., Ottolini, L. & Busà, T. (2001). Transition of Mount Etna lavas from a mantle-plume to an island-arc magmatic source. *Nature* **412**, 900–904.

Schleicher, J. M., Bergantz, G. W., Breidenthal, R. E. & Burgisser, A. (2016). Time scales of crystal mixing in magma mushes. *Geophysical Research Letters* **43**, 1543–1550.

Spilliaert, N., Allard, P., Métrich, N. & Sobolev, A. V. (2006). Melt inclusion record of the conditions of ascent, degassing and extrusion of volatile-rich alkali basalt during the powerful 2002 flank eruption of Mount Etna (Italy). *Journal of Geophysical Research* **111**, B04203.

Stevens, N. F., Murray, J. B. & Wadge, G. (1997). The volume and shape of the 1991–1993 lava flow field at Mount Etna, Sicily. *Bulletin of Volcanology* **58**, 449–454.

Tanguy, J. C. (1980). L'Etna: étude pétrologique et paléomagnetique: implications volcanologiques. PhD thesis, University of Paris, 618 pp.

Tanguy, J. C. & Clocchiatti, R. (1984). The etnean lavas, 1977–83: petrology and mineralogy. *Bulletin of Volcanology* **47**, 879–894.

Tanguy, J. C. & Patanè, G. (1996). *L'Etna et le monde des volcans*. Diderot.

Tanguy, J. C., Condomines, M., Le Goffe, M., Chillemi, V., La Delfa, S. & Patanè, G. (2007). Mount Etna eruptions of the last 2,750 years: revised chronology and location through archeomagnetic and ^{226}Ra–^{230}Th dating. *Bulletin of Volcanology* **70**, 55–83.

Ubide, T., Arranz, E., Lago, M., Galé, C. & Larrea, P. (2012). The influence of crystal settling on the compositional zoning of a thin lamprophyre sill: a multimethod approach. *Lithos* **132–133**, 37–49.

Ubide, T., Galé, C., Larrea, P., Arranz, E. & Lago, M. (2014). Antecrysts and their effect on rock compositions: the Cretaceous lamprophyre suite in the Catalonian Coastal Ranges (NE Spain). *Lithos* **206–207**, 214–233.

Ubide, T., McKenna, C. A., Chew, D. M. & Kamber, B. S. (2015). High-resolution LA-ICP-MS trace element mapping of igneous minerals: In search of magma histories. *Chemical Geology* **409**, 157–168.

Viccaro, M., Giacomoni, P. P., Ferlito, C. & Cristofolini, R. (2010). Dynamics of magma supply at Mt. Etna volcano (Southern Italy) as revealed by textural and compositional features of plagioclase phenocrysts. *Lithos* **116**, 77–91.

Viccaro, M., Calcagno, R., Garozzo, I., Giuffrida, M. & Nicotra, E. (2015). Continuous magma recharge at Mt. Etna during the 2011–2013 period controls the style of volcanic activity and compositions of erupted lavas. *Mineralogy and Petrology* **109**, 67–83.

Viccaro, M., Barca, D., Bohrson, W. A., D'Oriano, C., Giuffrida, M., Nicotra, E. & Pitcher, B. W. (2016a). Crystal residence times from trace element zoning in plagioclase reveal changes in magma transfer dynamics at Mt. Etna during the last 400 years. *Lithos* **248–251**, 309–323.

Viccaro, M., Giuffrida, M., Nicotra, E. & Cristofolini, R. (2016b). Timescales of magma storage and migration recorded by olivine crystals in basalts of the March–April 2010 eruption at Eyjafjallajökull volcano, Iceland. *American Mineralogist* **101**, 222–230.

Viccaro, M., Zuccarello, F., Cannata, A., Palano, M. & Gresta, S. (2016c). How a complex basaltic volcanic system works: constraints from integrating seismic, geodetic, and petrological data at Mount Etna volcano during the July–August 2014 eruption. *Journal of Geophysical Research: Solid Earth* **121**, 5659–5678.